Journal of Vacuum Science & Technology A

Conductive TiN thin films grown by Plasma-Enhanced Atomic Layer Deposition: Effects of N-sources and thermal treatments

Clémence Badie,[1] Héloïse Tissot,[1] Beniamino Sciacca,[1] Maïssa K. Barr,[2] Julien Bachmann,[2] Christophe Vallée,[3] Gaël Gautier,[4] Thomas Defforge,[4] Vincent Astie,[5] Jean-Manuel Decams,[5] Mikhael Bechelany,[6] and Lionel Santinacci[1]

[1)]*Aix Marseille Univ, CNRS, CINAM, France*
[2)]*Friedrich-Alexander-Universität Erlangen-Nürnberg, Chair Chemistry of Thin Film Materials, IZNF, Erlangen, Germany*
[3)]*SUNY Polytechnic Institute, CNSE, Albany, USA*
[4)]*GREMAN UMR-CNRS 7347, INSA Centre Val de Loire, Université de Tours, Tours, France*
[5)]*Annealsys SAS, 139 rue des Walkyries, Montpellier, France*
[6)]*Institut Européen des Membranes, IEM, UMR 5635, Univ Montpellier, CNRS, ENSCM, Montpellier, France*

(*Electronic mail: lionel.santinacci@cnrs.fr)

(Dated: 1 February 2023)

This work consists of optimizing TiN plasma-enhanced atomic layer deposition using two different N-sources: NH_3 and N_2. In addition to maximizing the growth per cycle (GPC) and to shorten the deposition duration, comprehensive in and ex situ physicochemical characterizations give valuable information about the influence of the N-source nature, their dilution in Ar and the plasma power on layer's final properties. N_2 and NH_3 dilutions within Ar are extensively investigated since they are critical to decreasing the mean free path (ℓ) of plasma-activated species. A 1:1 gas ratio for the N-sources:Ar mixture associated to low flows (20 sccm) are optimal values for achieving highest GPCs (0.8 Å/cycle). Due to lower reactivity and shorter ℓ of the excited species, N_2 plasma is more sensitive to power and generator-to-sample distance, this contributes to lower conformality than with NH_3 plasma. The resistivity of the initial amorphous films was high ($\geq 1000\,\mu\Omega$·cm) and were significantly reduced after a thermal treatment ($\leq 400\,\mu\Omega$·cm). This demonstrates clearly the beneficial effect of the crystallinity of the film conductivity. Though N_2 process appears slightly slower than NH_3 one, it leads to an acceptable film quality. It should be considered since it is non-harmful and the process could be further improved by using a reactor exhibiting an optimized geometry.

I. INTRODUCTION

Titanium nitride thin films are typically used in microelectronics for their metal-like electrical conductivity[1–3]. They can also constitute an efficient corrosion protection because they exhibit high thermal and chemical stabilities as well as good mechanical wear resistance for a relatively low cost[4]. Recently, TiN films have been used in other fields such as energy storage[5,6] or plasmonic[7]. Most of these applications request a homogeneous and pinhole-free layer that can accommodate the substrate topography. Atomic layer deposition (ALD) fulfills these requirements compared to physical and chemical vapor deposition (PVD and CVD) techniques[8–10]. Historically, halides and mostly $TiCl_4$ with NH_3 constitute the main precursor association to grow TiN exhibiting a satisfying film quality (i. e. low carbon contamination $\leq 5\%$ and low resistivity $\leq 1000\,\mu\Omega$·cm). These processes are performed at high temperatures (300 to 500°C)[11,12], that are not compatible with thermally sensitive substrates. In addition, the halide-based chemicals can be trapped within the deposit or back-react with the film and damage the pumping system. Organometallic compounds can be used at lower process temperatures (T_{ALD}) and they are less corrosive. They have thus been largely explored and have progressively become the most investigated Ti precursors. Few studies are dedicated to alkoxides (e. g. titanium tetraisopropoxide, TTIP[13]), because such oxygen containing ligands should be avoided to prevent oxygen contamination. Most of the literature focus on alkylamides such as tetrakis(dimethylamino)titanium (TDMAT), tetrakis(diethylamino)titanium (TDEAT), tetrakis(ethylmethylamino)titanium (TEMAT) or heteroleptic molecules such as biscyclopentadienyl titanium triisopropylguanidinate ($Cp_2Ti[(N^iPr)_2CN(H)^iPr]$)[14–19]. Among those organometallic precursors, TDMAT is currently the most used and investigated in research laboratories. The co-reactant should be sufficiently reactive to complete the ALD reaction by removing the ligands of chemisorbed metallic precursor to limit the contamination (i. e. ligands trapped into the film). Usually, NH_3 is used as N-source for thermal ALD process[20–23]. Hydrazine is presented as highly reactive alternative but it is also highly hazardous[24].

Plasma-enhanced ALD (PE-ALD) enables the use of supplementary co-reactants. N_2 and H_2 can indeed lead to nitrides when they are injected separately or as a mixture in a plasma-assisted process. This deposition mode has resulted in various nitride thin films such as InN[25], AlN[26], TaN_x[27,28], SiN_x[29], HfN_x[30], ZrN_x[30] and TiN[31–39]. Although NH_3 molecule exhibits high reactivity, several studies also report plasma-enhanced processes using this chemical because it may lead to reduced resistivity and contamination[40–42]. In PE-ALD mode, additional parameters such as the generation type (inductively or capacitively coupled plasma), the geometry (remote or direct), the applied plasma power (P_{plasma}), dilution and ratio of the pulsed gases as well as sample bias

can be adjusted. Comprehensive ex situ characterizations of the deposited films along with in situ analyses are therefore requested to get a better understanding of the parameter influence on the process and subsequently to improve the film quality. For instance, Krylov et al. demonstrated that minimizing the total plasma gases pressure (varying N_2 or NH_3 and Ar flows) is the key to obtain highly crystalline and low resistive TiN films ($\leq 100\,\mu\Omega$·cm)[38,43].

The present work is dedicated to optimizing the growth rate of TiN PE-ALD and to study the co-reactant influence on the film properties such as resistivity. In a previous study[44], we assessed conductivity and conformality of TiN films grown by thermal- and PE-ALD using TDMAT with NH_3 according to the recipes developed by the reactor manufacturer. Conformal films were deposited onto nanoporous anodic alumina (1:75) and resistivity $\leq 1000\,\mu\Omega$·cm was achieved on planar silicon. Here, a special attention is drawn on the understanding of the plasma-assisted step using two different N-sources, NH_3 and N_2, while the thermal-ALD process acts as reference. Using NH_3 plasma, N^* and H^* excited species will be generated, while using N_2, no reducing species (H^*) will be formed, only N^*. As mentioned above, NH_3 is intrinsically a highly reactive molecule, without plasma activation. Conversely, N_2 is an inert gas that does not lead to TiN growth by thermal-ALD (it is often used as vector gas in this mode). However, Krylov et al.[37,38,43] have reported that N_2 plasma activation can lead to TiN formation. They have also shown that using NH_3 instead of N_2 as well as by minimizing the gas flow (i. e. lower pressure) resulted to a higher crystallinity of the layers and, consequently, to a better conductivity. In addition, a slight improvement of the conductivity was also found when increasing P_{plasma} during the deposition process[38]. The present work attempts to discuss those results by in-depth studies of the influence of the gas flows and plasma power during the plasma-assisted step. Those investigations are coupled to comprehensive in and ex situ physico-chemical analyses of the TiN deposition on plane and structured surfaces.

The initial recipes optimization are performed by assessing the ALD sequence in order to improve the growth per cycle (GPC), to inject the appropriate amount of precursors and to shorten the process duration. Since it is well-documented, the first half-cycle, dedicated to Ti-source, is shortly described while the second half-cycle, devoted to N-source reaction, is deeply investigated. In situ spectroscopic ellipsometry (SE) and optical emission spectroscopy (OES) are respectively used to monitor GPC and to identify the plasma composition depending on the precursor chemistry, their dilution in the vector gas as well as the plasma power. Morphology, chemical composition, crystalline structure and electrical properties were studied after depositions and conformality was assessed on well-defined porous Si. The resistivity is then related to the deposition conditions and compared to the reference thermal process.

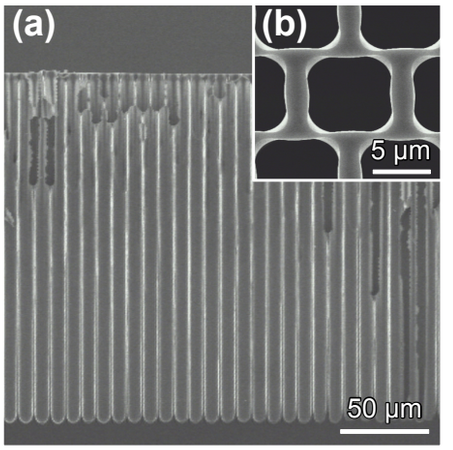

FIG. 1. SEM observations of bare ordered macropores: (a) cross section and (b) top view. Pores opening and length are respectively around 7 and 215 μm, that corresponds to an aspect ratio of 1:30.

II. EXPERIMENTS

A. Sample preparation and TiN deposition

TiN deposition was performed on n-type Si (100) (phosphorus doped, 1-10 Ω·cm, from Sil'tronix, France). The wafers were cut in $1\times1\,\text{cm}^2$ pieces and were degreased by sonicating in acetone, isopropanol, methanol, and ultra-pure water, followed by a dip in HF 5% for 30 s. All chemicals were analytical grade from Sigma Aldrich. The samples were then vigorously rinsed in ultra-pure water, dried under a nitrogen stream and stored in an Ar-filled glovebox.

The conformality of the TiN depositions was assessed on microstructured Si wafers. Fig. 1 presents ordered macropores grown on p-type Si (100) (boron doped, 30-50 Ω·cm) by an anodic etching performed in HF 5% and cetyltrimethylammonium chloride ($120\,\mu\text{g}\cdot\text{L}^{-1}$) at a constant current density of $15\,\text{mA}\cdot\text{cm}^2$ for 7 h. This process has been previously described in details[45].

Both thermal- and PE-ALD were carried out in a showerhead geometry reactor (Fiji 200, Veeco/Cambridge Nanotech) equipped with a remote inductive-coupled plasma source (Seren IPS Inc.), depicted in Fig. 2. During the PE-ALD processes, P_{plasma} was ranged from 50 to 300 W at 13.56 MHz. TDMAT (99.99%, Strem Chemicals) was used as Ti precursor with two different N-sources, NH_3 or N_2, associated with Ar as vector gas. All gases were electronic grade ($\geq$ 99.999%, from Linde Electronics). Ar was simultaneously flowed at solid/liquid and gaseous precursor inlets (see Fig. 2a). Ar flow (ϕ_{Ar}) at the gaseous precursor inlet (where plasma is generated) was varied (from 0 to 200 sccm) to adjust N-source dilution in the vector gas. The pumping system operated at its maximum during the depositions. The pressure (P) in the reactor was not regulated. It ranged from 0.1 to 0.3 Torr depending on the gas flows (ϕ_{Ar}, ϕ_{NH_3} and ϕ_{N_2} for Ar, NH_3 and N_2, respectively). TDMAT was maintained at 70°C and chamber temperature was varied from $T_{\text{ALD}} = 100$ to 300°C to screen

the ALD window. If not specified, $T_{ALD} = 200°C$. ALD sequences consist of pulsing and purging successively TDMAT and N-sources for defined durations (x_{Ti}:y_{Ti}:x_N:y_N). They are indicated in the following since optimization of the different processes are reported in the results section. The thickness of the films (t_{ALD}) was adjusted by varying the number of ALD cycles (N_{ALD}). For most of the depositions, wafers were positioned on the sample holder at the regular generator-to-sample distance (d_{plasma}) of 38.2 cm (Fig. 2a). In some cases, samples were lifted up using metallic cylinders to shorten d_{plasma}. As indicated on Fig. 2b, the shorter distances were 16.2 and 20.2 cm, respectively.

Some TiN films were encapsulated to prevent oxygen incorporation after air exposure during sample transportations. Thin ALD Al_2O_3 and TiO_2 layers exhibiting thicknesses of 10 and 5 nm, respectively, were grown directly after the TiN process at 150°C. Depositions of both oxides have been described previously[46,47]. In other cases, TiN layers were annealed under a reductive and nitriding atmosphere (N_2:H_2:NH_3, 480:60:60 sccm, respectively) using an AS-One furnace (Annealsys SAS) for 5 min at an annealing temperature (T_{an}) ranging from 600 to 800°C under $P = 50$ Torr. All samples were sealed in an Ar-filled container directly after deposition and annealing for storage and transportation (they were exposed to air less than a minute).

B. Characterizations

TiN thickness was monitored during deposition by in situ SE using a M-2000V (J. A. Woollam Co.). Curve fitting was performed using the CompleteEASE 5.10 software (model was assessed by comparing simulations to thickness measurements performed on TEM cross section observations). GPC was deduced from thickness measurements achieved by SE. The root mean square roughness (R_{RMS}) of the layers was measured by atomic force microscopy (AFM) using a XE-100 PSIA system by scanning a $5\times5\,\mu m^2$ area. Scanning and transmission electron microscopies (SEM and TEM) using a JSM 7900F (JEOL Ltd) and a JEM 2010 (JEOL Ltd), respectively, were used to investigate the morphology, confirm the thickness and assess the films conformality. Energy dispersive spectroscopy (EDS) was performed using a Quantax FlatQuad (Bruker). The TEM cross sections were carried out on samples prepared by ion milling with a precision ion polishing system (PIPS, Gatan M691).

Crystalline structure was analyzed by X-ray diffraction (XRD) using a high brilliancy rotating anode X-ray source (Rigaku RU 200BH) and a Xenocs Fox3D Cu 12_INF mirror (Osmic) coupled with an image plate detector (Mar345, Rayonix). The incident radiation was Cu K_α (1.5418 Å) exhibiting a $0.5 \times 0.5\,mm^2$ beam size.

X-ray photoelectron spectroscopy (XPS) was used to determine the film composition depending on their preparation procedure. Samples were studied after TiN deposition (as-grown, AG), after thermal treatment (annealed, An) and after protective encapsulation. The analyses were carried out on an ULVAC-PHI Quantera II system working at a base pressure of 7.5×10^{-7} Torr and equipped with a monochromated Al K_α source and a hemispherical energy analyzer. To prevent charging a combination of electron and ion neutralization was employed. Data processing was performed with CasaXPS analysis software (version 2.3.22PRO1.0) using a Shirley type background subtraction. The component peaks were defined by binding energy (BE), full width at half maximum (FWHM) and Gaussian-Lorentzian envelopes.

During TiN PE-ALD, plasma composition was monitored by in situ OES depending on injected N-source (NH_3 or N_2). Emitted light was collected at the plasma source (Fig. 2a) and analyzed between $\lambda = 360$ - 900 nm by an UV-vis spectrometer (Avaspec ULS 3648 USB2 from Avantes) driven by the Avasoft Full software. During OES measurements, the optical fiber was located at the plasma generator window because no sufficient light flux was collected at the lower window (closer to the sample).

To assess film quality, electrical measurements were performed on the TiN layers by evaporating successively 10/150 nm thick Cr/Au pads ($100 \times 80\,\mu m^2$, 100 μm-spaced). The resistivity was deduced from current-voltage curves obtained by 4-point probe (FPP) technique using a HP4140 PicoAmmeter/DC voltage source.

III. RESULTS AND DISCUSSION

A. Process optimization

As mentioned in the introduction, the three TiN ALD processes are investigated: thermal using NH_3 (*th*-NH_3) and plasma-assisted using NH_3 or N_2 (*pl*-NH_3 and *pl*-N_2, respectively) both mixed with Ar. Since thermal process optimization led to slight modifications of the initial ALD sequence, it is reported in Fig. S1 in supplementary materials (see supplementary material at URL will be inserted by AIP Publishing for additional process optimization data and characterizations). Conversely, investigations performed on PE-ALD processes result in strong improvements of the initial recipes that are deeply described in Table S1. Studies are therefore focused on the second half-cycle (plasma-assisted N-source reaction) while the first half-cycle of both plasma-enhanced processes (TDMAT reaction) is also depicted in Fig. S2 in supplementary materials. For all processes, saturation curves for TDMAT reveal an optimum pulse time of 0.2 s coupled with an 6 s-long purge that have been applied in the following. ALD windows of all processes before and after optimization is presented and discussed in Fig. S3 in supplementary materials. The ALD window for the three processes seems to be around $150 \leq T_{ALD} \leq 200°C$.

1. Effect of N-source dilution

The optimization of the two plasma-based recipes starts by studying the influence of N-source dilution within Ar. In initial recipe, Ar and NH_3 flows at plasma generator inlet are set to $\phi_{Ar} = 200$ and $\phi_{NH_3\,or\,N_2} = 70$ sccm, respectively. This

Journal of Vacuum Science & Technology A

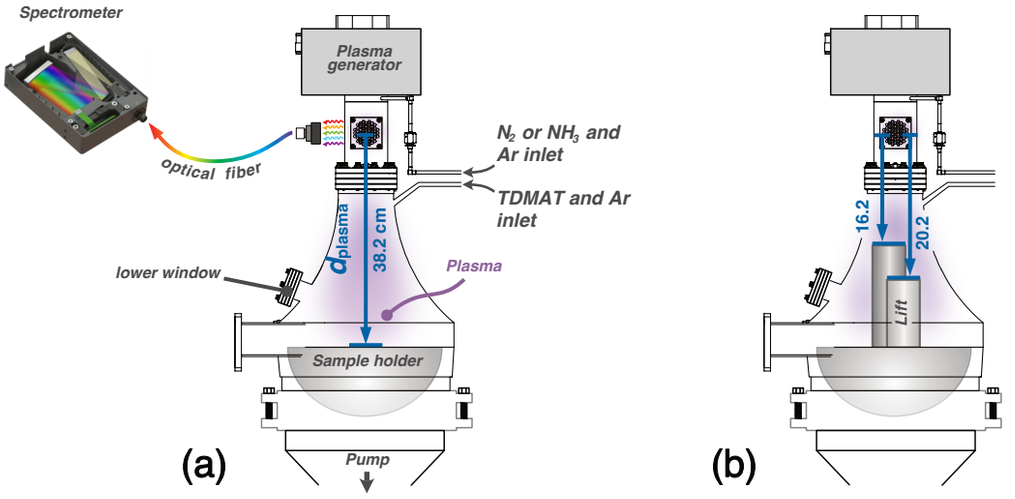

FIG. 2. Schematic drawings of the shower-head reactor (Fiji 200) and its main constituting components. (a) The sample is located at its regular position $d_{\text{plasma}} = 38.2$ cm and OES monitoring is shown near the plasma generator. (b) The sample position is lifted to shorten the plasma generator-to-sample distance: $d_{\text{plasma}} = 16.2$ or 20.2 cm.

situation is named *diluted conditions* in the following. It corresponds to a dilution ratio $\rho_\phi < 1$, with ρ_ϕ defined by Eq.1:

$$\rho_\phi = \frac{\phi_{NH_3}}{\phi_{Ar}} \quad \text{or} \quad \frac{\phi_{N_2}}{\phi_{Ar}} \tag{1}$$

Fig. 3a presents the influence of NH_3 dilution in Ar on GPC during the corresponding plasma processes. In diluted conditions, increasing ϕ_{NH_3} does not modify the GPC that remains almost constant around 0.6 Å/cycle (dark blue squares in Fig. 3a). The situation named *equal flow conditions* consists of setting co-reactant and vector gas flows to equal values: $\phi_{NH_3} = \phi_{Ar}$ then $\rho_\phi = 1$. In such situation, GPC significantly increases with ϕ_{NH_3} (dark blue circles on Fig. 3a). This behavior can be ascribed to the loss of pure ALD behavior due to a CVD contribution. When the *pl*-NH_3 purge is too short, TDMAT injected during the next ALD cycle can, indeed, react with the supplemental physisorbed species such as NH_3 or NH_3^*. To confirm this observation, the purge duration is extended to 20 s (light blue circles on Fig. 3a). This elongated evacuation step is then sufficient to remove all physisorbed species and GPC saturates around 0.85 Å/cycle when $\phi_{NH_3} \geq 20$ sccm. This indicates that, in equal flow conditions, to avoid CVD contribution, a pulse of 20 s must be associated to a 20 s purge instead of 5 s proposed in the initial recipe (Table S1). For lower flows ($\phi_{NH_3} < 20$ sccm), GPC is lower because not sufficient molecules are introduced to react with all available surface active sites.

Fig. 3c shows GPC evolution with ϕ_{NH_3} in diluted conditions for *th*-NH_3. It initially increases and reaches a plateau at 1 Å/cycle for $\phi_{NH_3} = 50$ sccm corresponding to surface active sites saturation. This evolution is different than equivalent *pl*-NH_3 exhibiting a constant GPC (dark blue squares on Fig. 3a). Although a similar NH_3 and Ar mixture is injected in the reactor at same temperature, ALD and PE-ALD do not exhibit similar GPC trends. To understand this difference, one has to consider the plasma properties. Species formed in this phase (i. e. ions, radicals, electrons) must travel from the generator to the surface. The mean free path (ℓ) is the distance covered by those species until they remain active. According to Eq. 2, ℓ decreases with P and d (kinetic diameter of the species).

$$\ell = \frac{kT}{\sqrt{2}\pi d^2 P} \tag{2}$$

When P increases, more collisions occur leading to recombinations into inert species, such as N_2 generated by NH_3^* collisions, ℓ is then reduced. This leads to a decreased number of excited species. High P can therefore be detrimental to the deposition. This is the case in diluted conditions in which P is almost twice as high as compared to equal flow conditions: $P = 0.31$ and 0.18 Torr, respectively, for $\phi_{NH_3} = 20$ sccm (see pressure profiles, Fig. S4, in supplementary materials). The mean free path should therefore decrease significantly. In addition, Ar is the main gas in the reactor ($\phi_{NH_3} < \phi_{Ar}$). This leads to a slower GPC and indicates that large NH_3 dilution within Ar is detrimental to deposition. Conversely, in equal flow conditions, for a similar ϕ_{NH_3}, P is lower, ℓ is extended and more excited NH_3^* species reach the surface and react. GPC is thus higher.

An analogous approach is applied to *pl*-N_2. Fig. 3b shows GPC evolution with ϕ_{N_2} in diluted and equal flow conditions. Similarly to *pl*-NH_3, diluted conditions lead to constant GPC around 0.6 Å/cycles, despite the ϕ_{N_2} increase (dark green squares on Fig. 3b). In contrast to *pl*-NH_3, under equal flow conditions ($\phi_{N_2} = \phi_{Ar}$), GPC is significantly higher (up to 1.2 Å/cycle) at low flows ($\phi_{N_2} \leq 20$ sccm) and it stabilizes around 0.6 Å/cycle for $\phi_{N_2} \geq 50$ sccm (dark green cir-

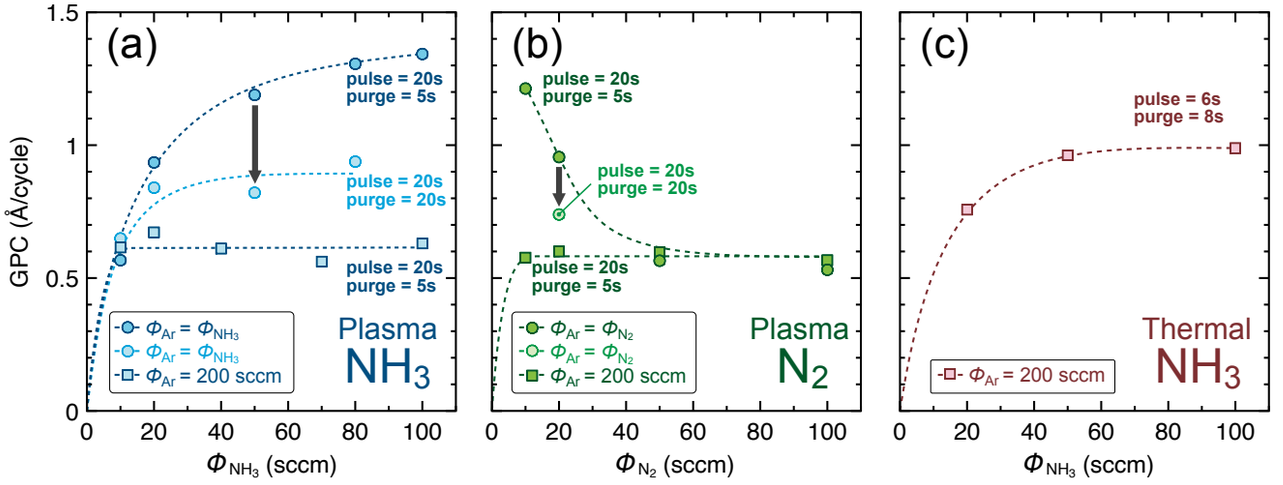

FIG. 3. Evolution of GPC depending on gas flow conditions for (a) *pl*-NH_3 and (b) *pl*-N_2. GPCs are plotted against (a) ϕ_{NH_3} and (b) ϕ_{N_2} under diluted (squares) and equal flow (circles) conditions. Purge time is varied from 5 to 20 s in equal flow conditions for *pl*-NH_3 and *pl*-N_2. (c) Evolution of GPC against ϕ_{NH_3} under diluted conditions for the reference *th*-NH_3 process. In all cases, ALD sequence is 0.2:6:x_N:y_N (x_N:y_N are indicated on the plots). Under diluted conditions $\phi_{Ar} = 200$ sccm.

cles Fig. 3b). Such results indicate that large ϕ_{N_2} seems also detrimental to generate excited N-species while at lower ϕ_{N_2}, reactive species undergo fewer collisions leading to a longer ℓ. High GPC values at low ϕ_{N_2} suggest a CVD contribution. When a longer purge (20 s) is applied, for $\phi_{N_2} = \phi_{Ar} = 20$ sccm, GPC indeed decreases to 0.7 Å/cycle because physisorbed reactants excess and/or byproducts are more efficiently pumped away (light green circles on Fig. 3b).

These results demonstrate that gas mixture composition is crucial to control both PE-ALD processes. In equal flow conditions, higher GPCs are observed because more excited N-species exhibiting longer ℓ are generated and travel toward the surface to react. Note that residence times of the species in the gas phase or at the surface have also been considered but it appears that ρ_ϕ and P are more likely to be the prevailing parameters (a detailed explanation is given in page 4 of supplemental materials).

Depending on N-source and vector gas flows, color changes are observed at the plasma generator window. A magenta light is emitted under diluted conditions that turns to blue-purple and light-pink when equal flows are injected for *pl*-NH_3/Ar and *pl*-N_2/Ar, respectively. Emissions at various wavelengths correspond to specific transitions. Magenta is attributed to Ar while blue and pink are ascribed to *pl*-NH_3 and *pl*-N_2, respectively[48]. In situ OES has thus been carried out during the plasma ignition to identify the created species.

Fig. 4 compares emission spectra measured in diluted and equal flow conditions for *pl*-NH_3 and *pl*-N_2. In the case of *pl*-NH_3 (Fig. 4a), significant variations are observed depending on ρ_ϕ. As expected, signals emitted by excited NH_3^* species are observed in any cases. Intense atomic hydrogen lines H_α and H_β are measured at $\lambda = 656$ and 486 nm, respectively, while peaks corresponding to N* species are almost merged in the background. As soon as Ar is injected in the reactor, emission peaks are measured at high wavelengths ($\lambda = 680$ to 880 nm). To quantify the emission of each gas, assuming that excitation coefficients (k_{NH_3} and k_{Ar}) do not depend on the discharge parameters (such as power, pressure, gas composition), we calculate, $R_{H/Ar}$, that corresponds to the ratio between the peak intensities of H_α and Ar($2p_1$) at $\lambda = 750$ nm (assuming k_{NH_3}/k_{Ar} constant):

$$R_{H/Ar} = \frac{I_H}{I_{Ar}} \tag{3}$$

In equal flow conditions, $R_{H/Ar} = 5.8$ while, in diluted conditions, it is significantly reduced to 2.2. Excited NH_3^* species signals seem to be enhanced in equal flow conditions with respect to pure *pl*-NH_3. The ratio between H_α and a residual peak at $\lambda = 757.6$ nm, taken as reference, is indeed 10% higher in equal flow compared to diluted conditions (see Table S2 in supplementary materials). Ar flow, i. e. dilution, is therefore a major parameter since it expands or dampens excited NH_3^* species emissions. At low ϕ_{Ar}, excited Ar^* as well as the numerous plasma generated electrons may indeed collide and transfer their energy to NH_3^* leading to enhanced emission. In diluted conditions, emissions arising from Ar excitations are conversely dominating. Since total pressure is high, many collisions and recombinations occur, then H_α and H_β peaks are quenched. A better reactivity and, consequently an optimized GPC are therefore expected in equal flow conditions.

Emission spectra variations in the case of *pl*-N_2 dilution is presented in Fig. 4b. *pl*-N_2 signals (molecular N_2 transitions, first and second positive system at $\lambda = 350$ to 450 nm and $\lambda = 530$ to 780 nm, respectively) are easily identified in equal flow conditions, $\phi_{N_2} = \phi_{Ar} = 20$ sccm (i. e. $\rho_\phi = 1$), whereas they almost disappear in diluted conditions. This evolution is very similar to *pl*-NH_3. Again, ϕ_{Ar} is beneficial at low values but becomes detrimental at high flows.

As mentioned above, when using remote plasma generator

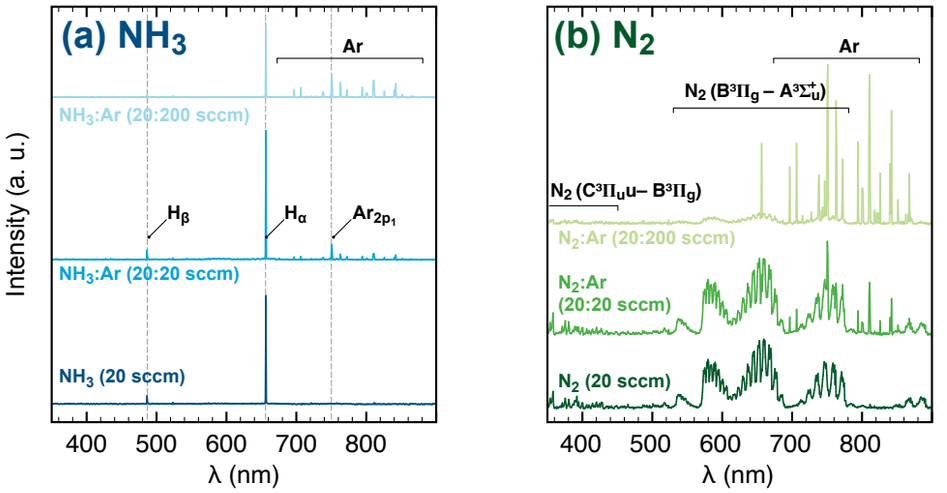

FIG. 4. OES spectra of (a) *pl*-NH_3 and (b) *pl*-N_2 pure or mixed within different Ar flows. Measurement are taken at the plasma generator window with P_{plasma}= 300 W using an acquisition time of 44 ms. The peaks have been identified according to literature[48–50].

geometry, reactions occur while excited species travel to the substrate. Since the OES measurements have been performed in the upper part of the chamber, they reveals reactive species that are produced at the generator and not necessarily those reaching the surface. This is especially suitable to optimize *pl*-N_2 process as it is an inert precursor without plasma activation. Assessing N-source flows and dilution give, however, valuable information about optimal conditions to promote reactive species transport from the generator to the surface. Ar dilution effect on GPC was also investigated for *pl*-NH_3 and *pl*-N_2. Fig. 5 shows the GPC evolution against ϕ_{Ar} while ϕ_{NH_3} and ϕ_{N_2} remain constant at 20 sccm. This corresponds to an increasing dilution in Ar. As expected from OES characterizations, GPC decreases with ϕ_{Ar} in both cases. It confirms that large dilution is detrimental to the film growth for both N-sources. However, at low dilution (i. e. $\phi_{Ar} \leq 20$ sccm), the presence of Ar does not influence significantly the GPC. A flow mixture of 20:20 sccm of both Ar and N-sources is then set as optimum in the following work.

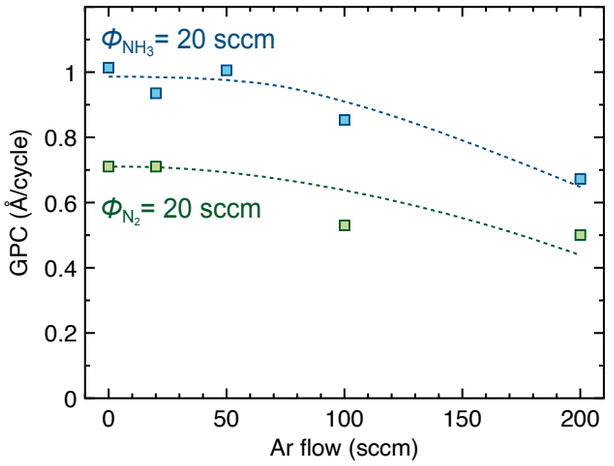

FIG. 5. Influence of dilution in Ar on both *pl*-NH_3 and *pl*-N_2. ϕ_{NH_3} and ϕ_{N_2} are constant at 20 sccm.

2. *Effect of N-sources pulse duration*

The pulse duration determines, as well as dilution, the amount of injected precursors into the reactor and indicates when saturation occurs. Its influence on GPC is studied for both *pl*-NH_3 and *pl*-N_2. Since maximal GPCs are measured in equal flow conditions at low flows, Fig. 6 presents GPC evolution against pulse duration with $\phi_{NH_3 \text{ or } N_2} = \phi_{Ar} = 20$ sccm. Fig. 6a shows GPC against *pl*-NH_3 pulse time. Corresponding GPC under diluted conditions is the horizontal dashed line at 0.6 Å/cycle plotted for comparison (dark blue dashed line). Measurements have been performed using 5 and 20 s-long purges (dark and light blue circles on Fig. 6a, respectively). In both cases, GPCs exhibit similar evolutions. They, first, increase steeply and, then, reach a plateau for a *pl*-NH_3 pulse of 5 s denoting that saturation is achieved. The highest GPC is around 1 Å/cycle with a 5 s purge (dark blue circles). However, CVD contribution should be considered for this short purge, since GPC drops significantly near 0.8 Å/cycle when a 20 s long purge (light blue circles) is applied. ALD conditions are, therefore, fulfilled when a 5 s pulse is associated to a 20 s purge but the overall cycle is long (31.2 s). 5 s purge is therefore selected to shorten the process (16.2 s). Although a *pl*-NH_3 pulse of 2 s does not lead to the highest GPC (saturation is not completely achieved), it is chosen to further shrink the total cycle duration (13.2 s). It also slightly compensates the possible CVD contribution while relatively high GPC of 0.86 Å/cycle is maintained. This balance is then chosen for the following work. The ALD sequence for *pl*-NH_3 is 0.2 : 6 : 2 : 5 s. It will be assessed by testing conformality on

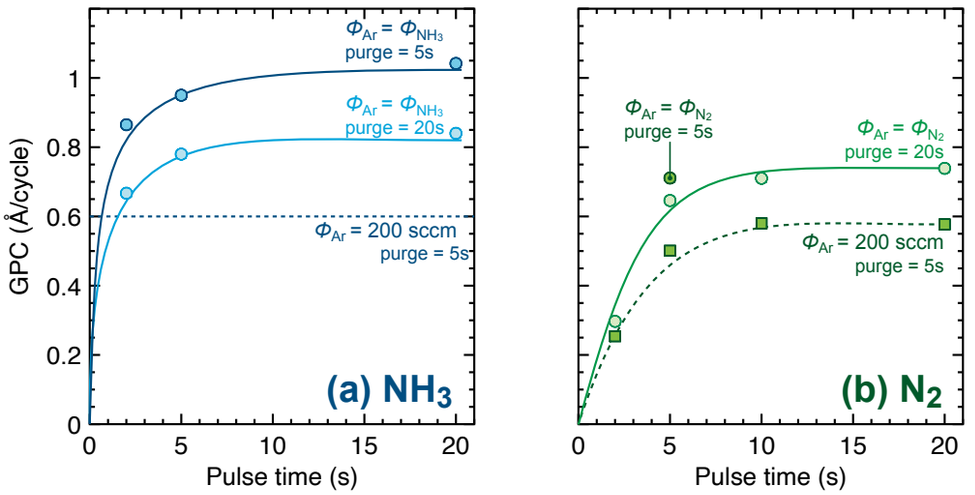

FIG. 6. (a) *pl*-NH_3 and (b) *pl*-N_2 pulses optimizations associate to purge duration. Circles and continuous lines correspond to equal flow conditions while squares and dashed lines stand for diluted conditions. The recipe used is 0.2:6:x_N:y_N s. N-source pulse times, x_N, correspond to abscissa while their purge times, y_N, are indicated on the plot.

high aspect ratio substrates thereinafter (Fig. 9).

Similarly, Fig. 6b presents the influence of *pl*-N_2 pulse duration on GPC. It is investigated under equal flow (light green circles) and diluted conditions are plotted as reference (dark green squares). As expected, GPC increases and stabilizes after pulsing 10 s in the two conditions. As already reported, dilution in Ar hinders film growth (dark green). The plateau is, indeed, around 0.5 Å/cycle when *pl*-N_2 is diluted while it is beyond 0.7 Å/cycle under equal flow conditions (light green). These results indicate that TiN grows in ALD regime for the 0.2 : 6 : 10 : 20 s sequence. As already proposed for *pl*-NH_3, pulse and purge are reduced to 5 s (dark green circle) to shorten the overall duration (from 36.2 down to 16.2 s) while keeping, as close as possible, deposition within ALD regime. In this case, saturation is almost reached, and CVD contribution is minor while GPC is maintained at a relatively high value 0.72 Å/cycle. The conformality of the films grown using the 0.2 : 6 : 5 : 5 s recipe is also evaluated thereinafter (Fig. 9).

3. *Effect of plasma power*

The plasma power is also a key parameter for PE-ALD. Its influence on deposition has thus been assessed on the whole range of the generator. Spectra shown in Fig. 7 indicate that, for both *pl*-NH_3 and *pl*-N_2, optical emission increases significantly with P_{plasma} but no strong spectra modifications are observed if power is increased from 100 to 300 W. This is further confirmed by comparing normalized spectra presented in Fig. S5 in supplementary materials. OES indicates that more excited species emitting light are generated, near the generator, when P_{plasma} is higher. However a direct correlation between emission intensity and number of species reacting at the surface cannot be established. As mentioned above, one has to consider other parameters such as P or ℓ. This is suggested when analyzing GPC evolutions with P_{plasma} for the two N-sources (Fig. 7c). In the case of *pl*-NH_3, a constant GPC near 0.8 Å/cycle is measured from 50 to 300 W while a progressive increase could be expected. It is explained by the intrinsic reactivity of NH_3 molecule that allows for ALD of TiN without plasma activation. A GPC of 0.44 Å/cycle is, indeed, observed under same conditions without plasma ignition (P_{plasma}= 0 W on Fig. 7c). It demonstrates that a thermal ALD component contributes to *pl*-NH_3 process. As soon as plasma is lightened (P_{plasma}= 50 W), GPC reaches a plateau because a small quantity of additional energy is sufficient to generate a large amount of excited species. It should be noted that without plasma-activation GPC is quite low as compared to optimized *th*-NH_3 shown in Fig. 3c (i. e. GPC = 0.76 Å/cycle at ϕ_{NH_3} = 20 sccm). This discrepancy comes from the different ALD time sequences of the two processes that are 2 and 6 s pulse for *pl*-NH_3 and *th*-NH_3 respectively. According to literature, PE-ALD can lead to higher GPC than thermal ALD[51,52]. Conversely, here, thermal mode exhibits a GPC near 1 Å/cycle whereas it is around 0.8 Å/cycle for plasma-enhanced process. Again, it could be ascribed to excited species recombinations into inert or less reactive molecules (e. g. N_2) during their transport to the surface: ℓ is smaller than the travelling distance (d_{plasma}). NH_3 molecule high reactivity and short ℓ also induce the saturation plateau observed in PE-ALD when P_{plasma} exceeds 50 W.

In the case of *pl*-N_2, GPC progressively increases with P_{plasma} corresponding to initial expectations (i. e. correlation between P_{plasma} and the reactive species amount). Since N_2 molecule is almost inert, no TiN growth is observed at P_{plasma} = 0 W (GPC = 0.07 Å/cyles). It demonstrates that deposition requires an assistance to proceed. Plasma ignition provides, indeed, a substantial amount of energy to excite N_2 molecules into N_2^* excited species. When P_{plasma} increases more excited species are generated (Fig. 7b) and, consequently, they can react at the surface. In opposition to *pl*-

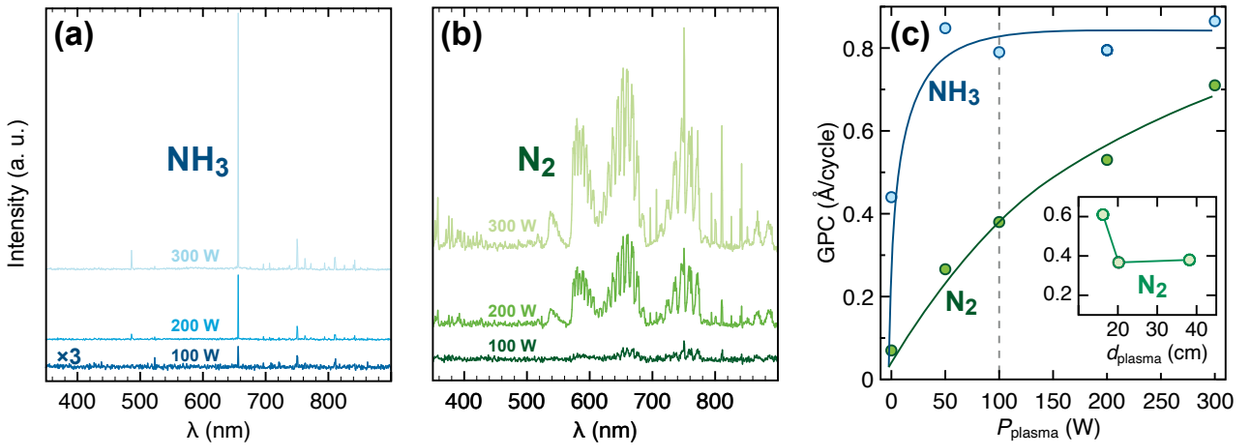

FIG. 7. OES spectra at different P_{plasma} for both (a) *pl*-NH_3 and (b) *pl*-N_2 mixed within Ar in equal flow conditions (ϕ_{NH_3} or $\phi_{N_2} = \phi_{Ar} = 20$ sccm and an acquisition time of 5 ms). Note that intensity of the *pl*-NH_3 spectrum at $P_{plasma} = 100$ W has been magnify (×3) for better reading. (c) Influence of P_{plasma} on GPC for *pl*-NH_3 and *pl*-N_2 processes under equal flow conditions (ϕ_{NH_3} or $\phi_{N_2} = \phi_{Ar} = 20$ sccm). Inset shows the dependence of GPC against d_{plasma} for *pl*-N_2 at P_{plasma}= 100 W (corresponding to the vertical dashed line on the main plot).

NH_3, no thermal-activated processes participate to the deposition with *pl*-N_2. A lower GPC is therefore observed and no saturation appears within the explored power range. It should occur at higher P_{plasma} but the present generator is limited to 300 W.

As described in experimental section (Fig. 2b), depositions at shorter distances (d_{plasma}= 16.2 and 20.2 cm) were compared to regular spacing (38.2 cm). Inset in Fig. 7c shows the GPC evolution with d_{plasma} at P_{plasma}= 100 W. GPC is the highest (0.61 Å/cycle) for the shortest distance, d_{plasma}= 16.2 cm and it decreases and reaches a plateau around 0.4 Å/cycle for longer d_{plasma}. It demonstrates that excited species are not reaching the surface because ℓ is significantly shorter than the regular generator-to-sample distance. According to Eq. 2, ℓ decreases with d^2. Since N_2 exhibits a larger kinetic diameter than NH_3 (d_{N_2} = 364 pm and d_{NH_3} = 260 pm), ℓ is expected to be twice shorter. This can partially explain the GPC gap between *pl*-NH_3 and *pl*-N_2 at regular sample position. Shortening d_{plasma}, reduces detrimental collision probability and increasing plasma power, at constant P, generates more excited species with an unchanged recombination rate. More excited species are able to reach the surface, GPC is therefore enhanced.

Since a P_{plasma} of 300 W was required to optimize *pl*-N_2, similar power was applied in the following *pl*-NH_3 to keep comparable conditions. For similar reasons, regular d_{plasma} was used in the following.

B. Characterizations of the films

In the previous section, plasma-assisted processes have been optimized depending on the N-source nature and then compared to the reference *th*-NH_3 deposition. In the following morphology, conformality, chemical composition, crystalline structure and electrical conductivity of films grown according to both PE-ALD are exhaustively investigated.

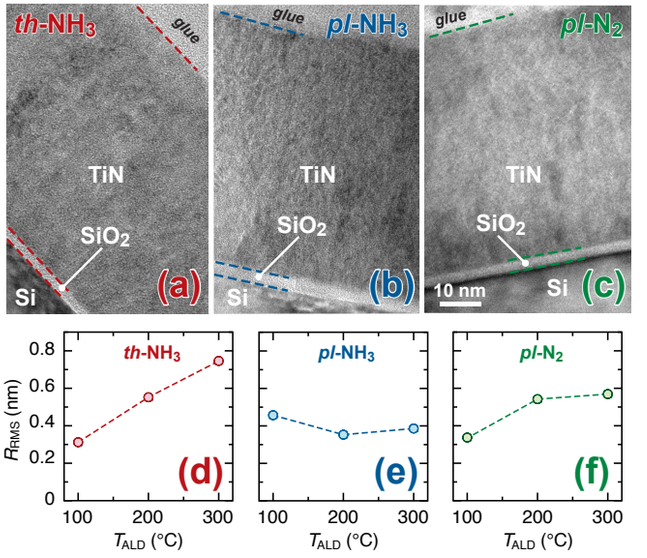

FIG. 8. TEM cross sections of TiN layers grown at T_{ALD} = 200°C for (a) *th*-NH_3, (b) *pl*-NH_3 and (c) *pl*-N_2. R_{RMS} of TiN layers measured by AFM after N_{ALD} = 100 cycles depending on T_{ALD} for (d) *th*-NH_3, (e) *pl*-NH_3 and (f) *pl*-N_2.

1. *Morphology and Conformality*

Film morphology has been observed before and after annealing under nitriding atmosphere. TEM cross sections of as-grown films are shown in Figs. 8a-c depending on the deposition methods. The films look very similar in all cases. Thickness measurements performed by SE are confirmed since deposits are as expected, 50 nm thick for N_{ALD} = 600 and

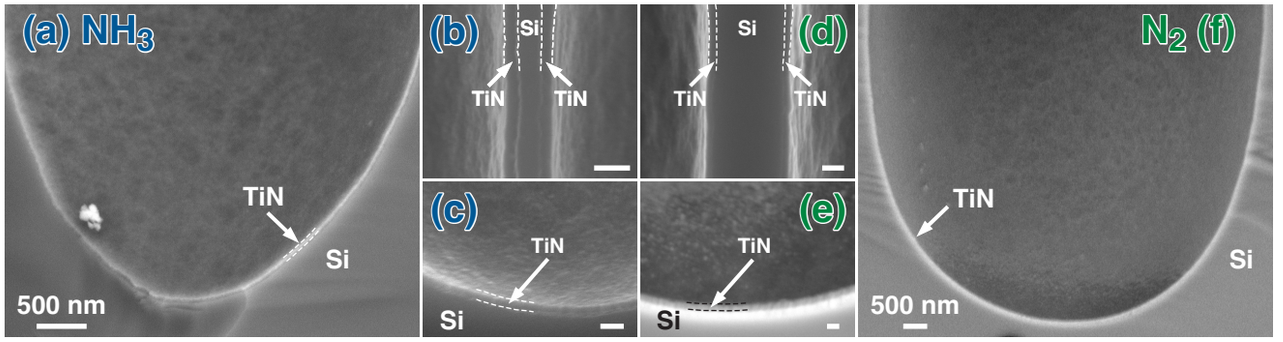

FIG. 9. SEM cross sections of porous Si coated by TiN lms: (a,b,c) *pl*-NH_3 and (d,e,f) *pl*-N_2. (a,f) show general views of pore tips while (b,e) and (c,d) show high magnication images of a single wall at half depth of the pore and at the pore tips, respectively. Scale bars in (b,c,d,e) correspond to 100 nm. Expected 50 nm-thick TiN layers grown at $T_{ALD} = 200°C$.

800 cycles for *pl*-NH_3 and *pl*-N_2, respectively. Compact, homogeneous and apparently crystallite-free layers are indeed observed on the three micrographs. Although a HF dip is performed before ALD, a 2 to 3 nm-thick SiO_2 interlayer is always visible. Fig. S6 in supplementary materials presents the annealed films at 700°C. No significant modifications are observed after thermal treatment under nitriding atmosphere. It suggests therefore no morphological variations of the layers.

Films roughness is measured by AFM. Evolutions of R_{RMS} against T_{ALD} are plotted on Figs. 8d-f. Measured values are relatively low (slightly higher than initial Si wafers roughness $R_{RMS} = 0.3$ nm) for all three routes ($0.3 < R_{RMS} < 0.8$ nm). It attests the film quality and the limited impact of T_{ALD} on the morphology. Thermal deposition shows a low linear increase with T_{ALD} (Fig. 8d) while both plasma processes exhibit almost no variation (Fig. 8e and Fig. 8f). In a previous study[44], we reported similar results. R_{RMS} increased with N_{ALD} for *th*-NH_3 while it was lower and constant for *pl*-NH_3. Plasma-activation could encourage the generation of smaller domains in greater numbers leading to smoother films as compared to the thermal activation.

As mentioned in experimental section, conformality tests have been carried out onto porous silicon exhibiting high aspect ratio of 1:30 (Fig.1). Figs. 9a-c present *pl*-NH_3 deposit at different locations of the substrates. Assaud et al. already reported conformal coating on anodic alumina membranes using initial *pl*-NH_3 recipe[44]. The optimized process should lead to compact and uniform coating onto such structured surfaces. Large-scale observation confirms the presence of TiN coating in the whole porous layer, verified by EDS analysis presented in Fig. S7 in supplementary materials. This is further evidenced by observing pore tips (Fig. 9a) and high magnification imaging performed at the pore wall and apex (Figs. 9b,c). Measured t_{ALD} is around 40 nm for a targeted value of 48 nm on planar Si wafer. A 2-s long *pl*-NH_3 pulse is therefore sufficient to coat such deep features and the short purge (5 s) does not degrade the conformality.

Figs. 9d-f present the corresponding layer grown using *pl*-N_2 for a similar targeted TiN thickness (t_{ALD}= 50 nm). Whereas whole pores are uniformly coated by *pl*-NH_3, Figs. 9e,f reveal a partial covering of the pore tips. There is clearly deposition at the apex but the film is not as homogeneous as using *pl*-NH_3. Nevertheless, on the walls (Fig. 9d) and the upper part of the pores, the deposit is compact. It exhibits a thickness near the expectation on planar Si wafer (around 42 nm). The film integrity is lost only in the tip vicinity. Since channels are very long ($> 200\,\mu$m), this effect can arise from the short pulse duration or it can also be ascribed to the short ℓ when *pl*-N_2 is used as predicted by Eq.2 (i. e. recombinations do not allow these species to reach the deepest part of the pores). Note also that potential CVD contribution induced by the short purge step (5 s) does not lead to localized TiN accumulation.

2. *Chemical composition*

The composition of the thin films is assessed by XPS. Figs. 10a-c compare Ti 2p spectra of as-grown films deposited by thermal ALD (AG-*th*-NH_3) and as-grown PE-ALD layers using *pl*-NH_3 and *pl*-N_2 (AG-*pl*-NH_3 and AG-*pl*-N_2, respectively) after a 5 min-long Ar-sputtering. In all cases, wide peak indicates several contributions. Ti 2p doublet peak decomposition reveals three contributions: (I) Ti–N from TiN around 455 eV, (II) Ti–O–N, ascribed to an oxygen placed in the TiN lattice (i. e. an oxynitride) around 456 eV and (III) Ti–O attributed to TiO_2 around 458 eV[53].

General Ti 2p peak shape measured for *pl*-N_2 indicates a larger TiN contribution compared to both NH_3-based processes (Fig. 10c). This is confirmed by semi-quantitative analysis presented in Table S3 in supplementary materials. No accurate stoichiometry has been calculated due to background uncertainty. The background shape hinders, indeed the modeling of the region between $2p_{3/2}$ and $2p_{1/2}$ components which leads to possible confusion when integrating the area of every contributions. Beside this restriction, all peaks were analyzed with the same conditions.

Since deposited films are oxynitrides rather to pure nitrides an annealing under nitriding and reductive atmosphere (NH_3 and H_2) is performed to convert the remaining oxide and oxinitride into nitride. Conditions are inspired from nitride synthesis method that consists in nitriding the correspond-

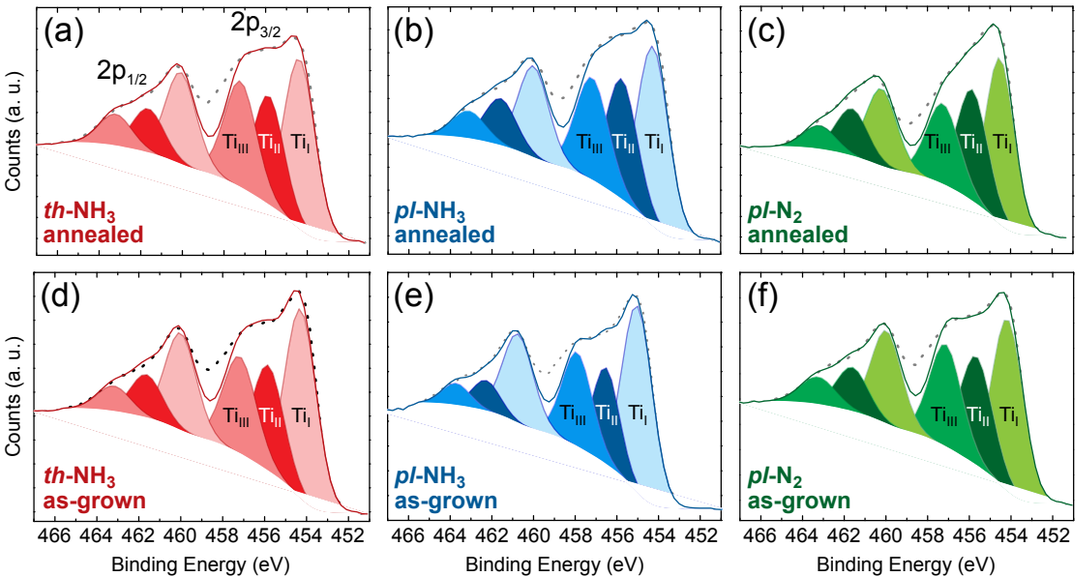

FIG. 10. Ti 2p XPS peaks from (a) *th*-NH_3, (b) *pl*-NH_3 and (c) *pl*-N_2 processes before and after annealing at $T_{an} = 700°C$ (d,e,f), respectively.

ing oxide. Usually, the process requires harsh conditions: $T_{an} \geq 700°C$ under NH_3 or N_2 flows. Several studies have been carried out to convert TiO_2 in TiN, mainly on powders[54,55]. Figs. 10d-f present Ti 2p spectra of corresponding films after nitriding at $T_{an} = 700°C$ for 5 min. TiN contribution appears slightly larger (see Table S3 in supplementary materials) but conversion of oxinitride and oxide contributions are not fully achieved. Survey spectra, N 1s and O 1s peaks of all three routes before and after annealing are depicted on Figs. S8-10 in supplementary materials.

The oxide contribution can arise from film oxidation in contact with air between the samples transportation from the ALD reactor to the furnace and to the XPS facility[56]. This is confirmed by XPS measurements performed on protected layers. A set of TiN films were encapsulated just after deposition by growing an Al_2O_3/TiO_2 bilayer at the top surface. XPS analysis has been carried out at different film depths using Ar sputtering. Fig. 11 presents *pl*-NH_3 case. As expected, the layer composition evolves from mostly an oxide, at the top surface, to an oxynitride in its bulk. Table S4 in supplementary materials summarize the %area of each element (Ti 2p, N 1s, O 1s and C 1s) for all three routes. Film encapsulation appeared to be an interesting technique to minimize the impact of sample transportation from ALD reactor to spectrometer. Nevertheless, to grow the protective Al_2O_3 layer, water pulses are used and could also cause film oxidation before the alumina film covers fully the TiN deposit. It is therefore difficult to conclude but the oxygen content decreases with Ar-sputtering suggests that film oxidation originates from an external source (capping layer deposition or environment). Thus, oxygen is inserted after deposition when the sample is exposed to air. In situ measurements are the most reliable technique in such situation. These analyses carried out on layers grown by ALD or other techniques have also observed an oxynitride and support the present findings (see e. g. Refs.[57–62]).

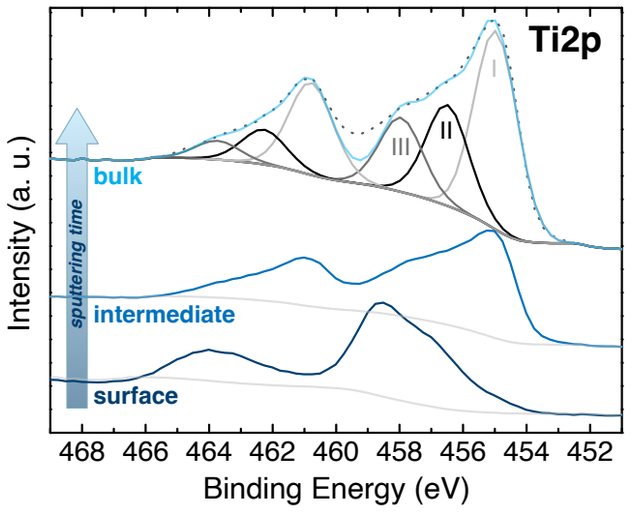

FIG. 11. XPS spectra of Ti2p peak from *pl*-NH_3 TiN film at different sputtering durations.

3. *Crystalline structure*

Fig. 12 presents diffractograms of the films before and after nitriding at $T_{an} = 600$, 700 and 800°C. Films grown by PE-ALD are mainly amorphous with a slight crystalline proportion and *pl*-NH_3 route seems to be slightly more crystalline than *pl*-N_2. Thermal process leads to more polycrystalline layers when deposition is carried out at $T_{ALD} \geq 200°C$. In all cases, after annealing, crystallinity increases, especially

for $T_{an} \geq 700$°C. Note that main diffraction peaks are not perfectly centered on the TiN reference (PDF 00-038-1420, black lines on Fig. 12) but mostly on the nearby TiO (PDF 00-008-0117, gray lines on Fig. 12). After annealing, peaks move closer to TiN references and are finally centered in between the two references. As discussed in section III.B.2, TiN surfaces are not stable in contact with air. They get therefore oxidized (Fig. 11) and diffractions peaks shift to a TiO compound[55,63]. In opposition to tetragonal anatase (PDF 00-021-1272), this compound exhibits a cubic structure like TiN, as well as a close lattice parameter. This is in agreement with XPS data (Tables S3, S4 in supplementary materials) since films are mainly oxynitrides even after annealing.

4. *Electrical properties*

Film quality is assessed by determining their resistivity throught FPP measurements on evaporated gold contacts. In literature, bulk TiN resistivity is around $20 \pm 10\,\mu\,\Omega$·cm while a resistivity $\leq 100\,\mu\,\Omega$·cm has been achieved using PE-ALD by Krylov et al.[38,43,64]. Investigation on the plasma power impact on the film resistivity presents no significant evolution for both *pl*-NH_3 and *pl*-N_2 processes in Fig. S11. Resistivities of as-grown and annealed films are displayed in Fig. 13. AG-*pl*-N_2 film is clearly the most resistive ($\approx 5000\,\mu\,\Omega$·cm). This can be due to its very low crystallinity. AG-*th*-NH_3 and AG-*pl*-NH_3 films present similar resistivities ($\approx 1300\,\mu\,\Omega$·cm) that are significantly lower. Compared to literature, these values are far from pure TiN. However, they remains relatively low for oxynitride films[12,17,20]. Thermal treatments in nitriding atmospheres significantly modify the resistivity. A strong decrease is, indeed, observed when $T_{an} \geq 700$°C. All layers exhibit then a resistivity in the range of 200 and 400 $\mu\,\Omega$·cm for *pl*-NH_3 and *pl*-N_2 processes, respectively. This can be related to the crystalline evolution at such temperature during annealing (crystallinity improvement reported in Fig. 12). Since TEM cross sections are not significantly different after annealing (Fig. S6), one can assume that crystalline domains remain in the nanometer scale embedded in amorphous TiN_xO_y matrix. Though conduction channels are created during this structural film modification. Those charge pathways are most likely to be grains boundaries as proposed by Lin et al.[65] on polycrystalline TiN_x films grown by magnetron sputtering. Since the composition does not evolve drastically after annealing, it seems it has no strong effect on the variation of the conductivity of the films.

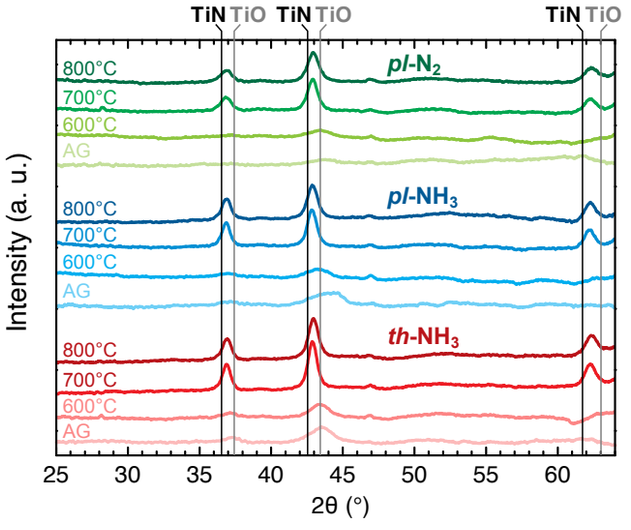

FIG. 12. XRD patterns of as-grown layers and their evolution with annealing temperature for the three deposition routes. Annealing in N_2, NH_3 and H_2 mixture for 5 min at $T_a = 600$, 700 and 800°C. Black and gray vertical lines correspond to TiN and TiO references, respectively.

IV. CONCLUSION

After optimizing the recipe (pulse/purge durations, gas flows, dilution and plasma power) and shortening the process duration, valuable information about deposition processes have been reported. First, as-grown films are not pure TiN but a mixture mainly composed of TiN and TiN_xO_y. XPS analysis coupled to reductive annealing or capping experiments tends to demonstrate that oxygen present in the layers is most probably incorporated after the deposition. The reductive annealing acts only as a thermal treatment that crystallizes the film.

The present study demonstrates also that gas mixture composition is crucial during both PE-ALD processes. The combined use of SE and OES is, indeed, highly efficient to study the effect of reactive gas dilution in the vector gas as well as the influence of P_{plasma}. Dilution is seldom taken into account in recipes and the present methodology could, therefore, successfully be applied to many other PE-ALD processes. Here, it is demonstrated that dilution and chamber pressure are crucial parameters since they can be strongly detrimental to the deposition. Their effect on ℓ is critical since they can induce

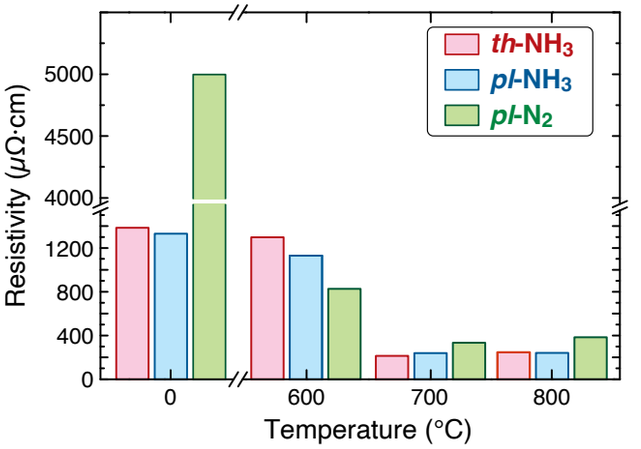

FIG. 13. Resistivity of TiN films grown by thermal- and PE-ALD (300 W, $\phi_{N-surce} = \phi_{Ar} = 20$ sccm, $P = 0.16$ Torr) and effect of different annealings. TiN films were ≈ 50 nm thick.

deleterious collisions of the reactive species causing a low GPC. Equal flow conditions and a relatively low P are found to be the most efficient conditions for both *pl*-N_2 and *pl*-NH_3 processes.

As reported earlier in literature,[37,38,43] NH_3 exhibits a higher reactivity than N_2. For NH_3, we show that plasma-activation is effective at low applied power and deposition saturates quickly for higher values. A small plasma-activation is sufficient because a non-negligible thermal activation contributes to *pl*-NH_3. Conversely, a large P_{plasma} is required in *pl*-N_2 since this N-source is inert without plasma. A shorter ℓ is also evidenced for N_2. The difference in reactivity between NH_3 and N_2 must therefore be put into perspective. Indeed, when using a shorter generator-to-sample distance, *pl*-N_2 is very similar to *pl*-NH_3. This demonstrates the significance of the reactor design.

Although PE-ALD is often not considered to be suitable for step edge decoration, conformal depositions using *pl*-NH_3 and *pl*-N_2 are achieved on porous Si exhibiting a 1:30 aspect ratio. A better uniformity is, nevertheless, reached with *pl*-NH_3. It could be explained by the lower reactivity of *pl*-N_2 and/or its shorter ℓ. However, this last consideration about ℓ has been obtained on planar surfaces. It should therefore be confirmed in specific pore geometry as it is difficult to establish a direct extrapolation of recombination phenomena occurring within channels since, there, gas flows and collisions can be strongly affected by the molecule confinement or depletion.

Since this work deals with TiN_xO_y instead of pure TiN films, the measured conductivities are, obviously, not as high as pure nitrides ($\leq 500\,\mu\Omega\cdot$cm). Annealing treatments demonstrate clearly the critical effect of the crystallinity on the conductivity. In previous reports,[37,38] the best conductivities were ascribed to the improvement of the crystalline structure of columnar layers. Here, the relation between crystallinity and conductivity is further obvious because as-grown samples are amorphous and they show a very high resistivity while, after annealing, they become crystalline and they turn to be significantly more conductive ($\leq 400\,\mu\Omega\cdot$cm).

In the end, conformal conductive thin films are efficiently grown in a shortened experimental time. Further improvement could be achieved by using a reactor design exhibiting a smaller plasma generator-to-sample distance (especially for *pl*-N_2) and a better analysis of the plasma composition near the surface should be completed if OES measurements are performed closer to the sample.

ACKNOWLEDGMENTS

D. Chaudanson, A. Altie, V. Heresanu, B. Demirdjian, S. Lavandier, F. Bedu (CNRS) are acknowledged for their precious help within electronic microscopy, x-ray diffraction, OES, contacts deposition and electric measurements. The authors acknowledge the financial support of the French Agence Nationale de la Recherche (ANR) under grant ANR-17-CE09-0049-03 (project MENINA). The French research network RAFALD (GDR CNRS) is also acknowledged for lending the first OES spectrometer.

DATA AVAILABILITY STATEMENT

The data that support the findings of this study are available from the corresponding authors upon reasonable request.

AUTHOR DECLARATIONS

Conflict of Interest

The authors have no conflicts to disclose.

REFERENCES

[1] H. C. M. Knoops, L. Baggetto, E. Langereis, M. C. M. van de Sanden, J. H. Klootwijk, F. Roozeboom, R. A. H. Niessen, P. H. L. Notten, and W. M. M. Kessels, "Deposition of TiN and TaN by Remote Plasma ALD for Cu and Li Diffusion Barrier Applications," J. Electrochem. Soc. **155**, G287 (2008).
[2] M.-D. Cheng, T. Luoh, C.-T. Su, T.-H. Yang, K.-C. Chen, and C.-Y. Lu, "Improvement of the properties and electrical performance on TiCl4-based TiN film using sequential flow chem. vap. deposition process," Thin Solid Films **518**, 2285–2289 (2010).
[3] A. Shearrow, G. Koolstra, S. J. Whiteley, N. Earnest, P. S. Barry, F. J. Heremans, D. D. Awschalom, E. Shirokoff, and D. I. Schuster, "Atomic layer deposition of titanium nitride for quantum circuits," Appl. Phys. Lett. **113**, 212601 (2018).
[4] J.-Z. Kong, P. Xu, Y.-Q. Cao, A.-D. Li, Q.-Z. Wang, and F. Zhou, "Improved corrosion protection of CrN hard coating on steel sealed with TiO_xN_y-TiN composite layers," Surf. Coat. Technol. **381**, 125108 (2020).
[5] P. Banerjee, I. Perez, L. Henn-Lecordier, S. B. Lee, and G. W. Rubloff, "Nanotubular metal-insulator-metal capacitor arrays for energy storage," Nature Nanotechnology **4**, 292–296 (2009).
[6] Y. Gao, J. Park, and X. Liang, "Synergic Titanium Nitride Coating and Titanium Doping by Atomic Layer Deposition for Stable- and High-Performance Li-Ion Battery," J. Electrochem. Soc. **165**, A3871–A3877 (2018).
[7] D. Fomra, M. Mamun, K. Ding, V. Avrutin, Ü. Özgür, and N. Kinsey, "Plasmonic colors in titanium nitride for robust and covert security features," Opt. Express **29**, 19586 (2021).
[8] M. Leskelä and M. Ritala, "Atomic layer deposition (ALD): from precursors to thin film structures," Thin Solid Films **409**, 138–146 (2002).
[9] R. W. Johnson, A. Hultqvist, and S. F. Bent, "A brief review of atomic layer deposition: from fundamentals to applications," Mater. Today **17**, 236–246 (2014).
[10] A. S. Asundi, J. A. Raiford, and S. F. Bent, "Opportunities for Atomic Layer Deposition in Emerging Energy Technologies," ACS Energy Lett. **4**, 908–925 (2019).
[11] M. Ritala, M. Leskelä, E. Rauhala, and J. Jokinen, "Atomic Layer Epitaxy Growth of TiN Thin Films from TiI_4 and NH_3," J. Electrochem. Soc. **145**, 2914–2920 (1998).
[12] C. H. Ahn, S. G. Cho, H. J. Lee, K. H. Park, and S. H. Jeong, "Characteristics of TiN thin films grown by ALD using $TiCl_4$ and NH_3," Met. Mater. Int. **7**, 621–625 (2001).
[13] M. Sowińska, S. Brizzi, C. Das, I. Kärkkänen, J. Schneidewind, F. Naumann, H. Gargouri, K. Henkel, and D. Schmeißer, "Analysis of nitrogen species in titanium oxynitride ALD films," Appl. Surf. Sci. **381**, 42–47 (2016).
[14] J.-S. Min, Y.-W. Son, W.-G. Kang, S.-S. Chun, and S.-W. Kang, "Atomic Layer Deposition of TiN Films by Alternate Supply of Tetrakis(ethylmethylamino)-Titanium and Ammonia," Japanese J. Appl. Phys. **37**, 4999–5004 (1998).
[15] L. A. Okada and S. M. George, "Adsorption and desorption kinetics of tetrakis(dimethylamino)titanium and dimethylamine on TiN surfaces," Appl. Surf. Sci. **137**, 113 (1999).

Journal of Vacuum Science & Technology A

[16]J.-Y. Yun, "Comparison of Tetrakis(dimethylamido)titanium and Tetrakis(diethylamido)titanium as Precursors for Metallorganic Chemical Vapor Deposition of Titanium Nitride," J. Electrochem. Soc. **146**, 1804 (1999).

[17]P. Caubet, T. Blomberg, R. Benaboud, C. Wyon, E. Blanquet, J.-P. Gonchond, M. Juhel, P. Bouvet, M. Gros-Jean, J. Michailos, C. Richard, and B. Iteprat, "Low-Temperature Low-Resistivity PEALD TiN Using TDMAT under Hydrogen Reducing Ambient," J. Electrochem. Soc. **155**, H625 (2008).

[18]Y. A. Wasslen, E. Tois, S. Haukka, K. A. Kreisel, G. P. A. Yap, M. D. Halls, and S. T. Barry, "A Family of Heteroleptic Titanium Guanidinates: Synthesis, Thermolysis, and Surface Reactivity," Inorg. Chem. **49**, 1976–1982 (2010).

[19]Z. Chen, X. Li, W.-M. Li, and G.-Q. Lo, "Plasma-Enhanced Atomic Layer Deposition (PEALD) of TiN using the Organic Precursor Tetrakis(ethylmethylamido)Titanium (TEMAT)," MATEC Web of Conferences **39**, 01010 (2016).

[20]J. Elam, M. Schuisky, J. Ferguson, and S. George, "Surface chemistry and film growth during TiN atomic layer deposition using TDMAT and NH_3," Thin Solid Films **436**, 145–156 (2003).

[21]F. Fillot, T. Morel, S. Minoret, I. Matko, S. Maîtrejean, B. Guillaumot, B. Chenevier, and T. Billon, "Investigations of titanium nitride as metal gate material, elaborated by metal organic atomic layer deposition using TDMAT and NH_3," Microelectron. Eng. **82**, 248–253 (2005).

[22]A. Dube, M. Sharma, P. F. Ma, P. A. Ercius, D. A. Muller, and J. R. Engstrom, "Effects of Interfacial Organic Layers on Nucleation, Growth, and Morphological Evolution in Atomic Layer Thin Film Deposition," J. Phys. Chem. C **111**, 11045–11058 (2007).

[23]D. Longrie, D. Deduytsche, J. Haemers, P. F. Smet, K. Driesen, and C. Detavernier, "Thermal and Plasma-Enhanced Atomic Layer Deposition of TiN Using TDMAT and NH_3 on Particles Agitated in a Rotary Reactor," ACS Appl. Mater. Interfaces **6**, 7316–7324 (2014).

[24]D. Alvarez, J. Spiegelman, R. Holmes, K. Andachi, M. Raynor, and H. Shimizu, "Ultra-High Purity Hydrazine Delivery for Low Temperature Metal Nitride ALD," ECS Trans. **77**, 219–225 (2017).

[25]A. Haider, S. Kizir, and N. Biyikli, "Low-temperature self-limiting atomic layer deposition of wurtzite InN on Si(100)," AIP Adv. **6**, 045203 (2016).

[26]K.-H. Kim, N.-W. Kwak, and S. H. Lee, "Fabrication and properties of aln film on gan substrate by using remote plasma atomic layer deposition method," Electron. Mater. Lett. **5**, 83–86 (2009).

[27]H.-S. Chung, J.-D. Kwon, and S.-W. Kang, "Plasma-Enhanced Atomic Layer Deposition of TaN Thin Films Using Tantalum-Pentafluoride and N_2/H_2/Ar Plasma," J. Elecrochem. Soc. **153**, C751 (2006).

[28]E. Langereis, H. C. M. Knoops, A. J. M. Mackus, F. Roozeboom, M. C. M. van de Sanden, and W. M. M. Kessels, "Synthesis and *in situ* characterization of low-resistivity TaN_x films by remote plasma atomic layer deposition," J. Appl. Phys. **102**, 083517 (2007).

[29]N. Leick, J. M. Huijs, R. A. Ovanesyan, D. M. Hausmann, and S. Agarwal, "Surface reactions of aminosilane precursors during N_2 plasma-assisted atomic layer deposition of SiN_x," Plasma Processes Polym. **16**, 1900032 (2019).

[30]I. Krylov, V. Korchnoy, X. Xu, K. Weinfeld, E. Yalon, D. Ritter, and M. Eizenberg, "Electrical and structural properties of conductive nitride films grown by plasma enhanced atomic layer deposition with significant ion bombardment effect," J. Appl. Phys. **128**, 065301 (2020).

[31]J. Y. Kim, Y. Kim, and H. Jeon, "Characteristics of TiN films deposited by remote plasma-enhanced atomic layer deposition method," Jpn. J. Appl. Phys. **42**, L414–L416 (2003).

[32]E. Langereis, S. B. S. Heil, M. C. M. van de Sanden, and W. M. M. Kessels, "*In situ* spectroscopic ellipsometry study on the growth of ultrathin TiN films by plasma-assisted atomic layer deposition," J. Appl. Phys. **100**, 023534 (2006).

[33]J. Musschoot, Q. Xie, D. Deduytsche, S. Van den Berghe, R. Van Meirhaeghe, and C. Detavernier, "Atomic layer deposition of titanium nitride from TDMAT precursor," Microelectron. Eng. **86**, 72–77 (2009).

[34]N. Samal, H. Du, R. Luberoff, K. Chetry, R. Bubber, A. Hayes, and A. Devasahayam, "Low-temperature ($\leq$200∘c) plasma enhanced atomic layer deposition of dense titanium nitride thin films," J. Vac. Sci. Technol., A **31**, 01A137 (2013).

[35]M. Burke, A. Blake, I. M. Povey, M. Schmidt, N. Petkov, P. Carolan, and A. J. Quinn, "Low sheet resistance titanium nitride films by low-temperature plasma-enhanced atomic layer deposition using design of experiments methodology," J. Vac. Sci. Technol., A **32**, 031506 (2014).

[36]M. Sowińska, K. Henkel, D. Schmeißer, I. Kärkkänen, J. Schneidewind, F. Naumann, B. Gruska, and H. Gargouri, "Plasma-enhanced atomic layer deposition of titanium oxynitrides films: A comparative spectroscopic and electrical study," J. Vac. Sci. Technol., A **34**, 01A127 (2016).

[37]I. Krylov, X. Xu, E. Zoubenko, K. Weinfeld, S. Boyeras, F. Palumbo, M. Eizenberg, and D. Ritter, "Role of reactive gas on the structure and properties of titanium nitride films grown by plasma enhanced atomic layer deposition," J. Vac. Sci. Technol., A **36**, 06A105 (2018).

[38]I. Krylov, E. Zoubenko, K. Weinfeld, Y. Kauffmann, X. Xu, D. Ritter, and M. Eizenberg, "Obtaining low resistivity ($\approx$100 μ ω·cm) TiN films by plasma enhanced atomic layer deposition using a metalorganic precursor," J. Vac. Sci. Technol., A **36**, 051505 (2018).

[39]S. Belahcen, C. Vallée, A. Bsiesy, A. Chaker, M. Jaffal, T. Yeghoyan, and M. Bonvalot, "Control of ion energy during plasma enhanced atomic layer deposition: A new strategy for the modulation of TiN growth delay on SiO_2," J. Vac. Sci. Technol. A **39**, 012410 (2021).

[40]S.-H. Kwon, O.-K. Kwon, J.-S. Min, and S.-W. Kang, "Plasma-enhanced atomic layer deposition of ru–TiN thin films for copper diffusion barrier metals," J. Electrochem. Soc. **153**, G578 (2006).

[41]H. C. M. Knoops, T. Faraz, K. Arts, and W. M. M. E. Kessels, "Status and prospects of plasma-assisted atomic layer deposition," J. Vac. Sci. Technol., A **37**, 030902 (2019).

[42]C. Vallée, M. Bonvalot, S. Belahcen, T. Yeghoyan, M. Jaffal, R. Vallat, A. Chaker, G. Lefèvre, S. David, A. Bsiesy, N. Possémé, R. Gassilloud, and A. Granier, "Plasma deposition—Impact of ions in plasma enhanced chem. vap. deposition, plasma enhanced atomic layer deposition, and applications to area selective deposition," J. Vac. Sci. Technol., A **38**, 033007 (2020).

[43]I. Krylov, X. Xu, Y. Qi, K. Weinfeld, V. Korchnoy, M. Eizenberg, and D. Ritter, "Effect of the substrate on structure and properties of titanium nitride films grown by plasma enhanced atomic layer deposition," Journal of Vacuum Science & Technology A **37**, 060905 (2019).

[44]L. Assaud, K. Pitzschel, M. Hanbücken, and L. Santinacci, "Highly-Conformal TiN Thin Films Grown by Thermal and Plasma-Enhanced Atomic Layer Deposition," ECS J. Solid State Sci. Technol. **3**, P253–P258 (2014).

[45]T. Defforge, M. Diatta, D. Valente, F. Tran-Van, and G. Gautier, "Role of Electrolyte Additives during Electrochemical Etching of Macropore Arrays in Low-Doped Silicon," J. Electrochem. Soc. **160**, H247–H251 (2013).

[46]M. Dufond, M. W. Diouf, C. Badie, C. Laffon, P. Parent, D. Ferry, D. Grosso, J. C. S. Kools, S. D. Elliott, and L. Santinacci, "Quantifying the Extent of Ligand Incorporation and the Effect on Properties of TiO_2 Thin Films Grown by Atomic Layer Deposition Using an Alkoxide or an Alkylamide," Chem. Mater. **32**, 1393–1407 (2020).

[47]P. Roy, C. Badie, J.-B. Claude, A. Barulin, A. Moreau, J. Lumeau, M. Abbarchi, L. Santinacci, and J. Wenger, "Preventing Corrosion of Aluminum Metal with Nanometer-Thick Films of Al_2O_3 Capped with TiO_2 for Ultraviolet Plasmonics," ACS Appl. Nano Mater. **4**, 7199–7205 (2021).

[48]R. W. B. Pearse and A. G. Gaydon, "The identification of molecular spectra," J. Chem. Educ. **41**, A398 (1964).

[49]A. J. M. Mackus, S. B. S. Heil, E. Langereis, H. C. M. Knoops, M. C. M. van de Sanden, and W. M. M. Kessels, "Optical emission spectroscopy as a tool for studying, optimizing, and monitoring plasma-assisted atomic layer deposition processes," J. Vac. Sci. Technol., A **28**, 77–87 (2010).

[50]E. H. Lock, R. F. Fernsler, S. Slinker, and S. G. Walton, "Experimental and Theoretical Estimation of Excited Species Generation in Pulsed Electron Beam–Generated Plasmas Produced in Pure Argon, Nitrogen, Oxygen, and Their Mixtures," NRL Memo. Rep. **6750-11-9333** (2011).

[51]H. B. Profijt, S. E. Potts, M. C. M. van de Sanden, and W. M. M. Kessels, "Plasma-Assisted Atomic Layer Deposition: Basics, Opportunities, and Challenges," J. Vac. Sci. Technol., A **29**, 050801 (2011).

[52]C. Detavernier, J. Dendooven, D. Deduytsche, and J. Musschoot, "Thermal Versus Plasma-Enhanced ALD: Growth Kinetics and Conformality," in *ECS Trans.*, Vol. 16 (ECS, Honolulu, HI, 2008) pp. 239–246.

[53]D. Gall, R. T. Haasch, N. Finnegan, T.-Y. Lee, C.-S. Shin, E. Sammann, J. E. Greene, and I. Petrov, "*In situ* X-ray Photoelectron, Ultraviolet Photoelectron, and Auger Electron Spectroscopy Spectra from First-Row

Transition-Metal Nitrides: ScN, TiN, VN, and CrN," Surf. Sci. Spectra **7**, 167–168 (2000).

[54]U. Guler, D. Zemlyanov, J. Kim, Z. Wang, R. Chandrasekar, X. Meng, E. Stach, A. V. Kildishev, V. M. Shalaev, and A. Boltasseva, "Plasmonic Titanium Nitride Nanostructures via Nitridation of Nanopatterned Titanium Dioxide," Adv. Opt. Mater. **5**, 1600717 (2017).

[55]H. Alhussain, T. Mise, Y. Matsuo, H. Kiyono, K. Nishikiori, and T. Akashi, "Influence of ammonia gas exposure on microstructure of nanocrystalline titanium nitride powder synthesized from titanium dioxide," J. Ceram. Soc. Jpn. **127**, 824–829 (2019).

[56]S. G. Park and D.-H. Kim, "Stability of Plasma Posttreated TiN Films Prepared by Alternating Cyclic Pulses of Tetrakis-Dimethylamido-Titanium and Ammonia," Japanese J. Appl. Phys. **43**, 303–304 (2004).

[57]C. Ernsberger, J. Nickerson, A. E. Miller, and J. Moulder, "Angular resolved x-ray photoelectron spectroscopy study of reactively sputtered titanium nitride," J. Vac. Sci. Technol., A **3**, 2415–2418 (1985).

[58]N. C. Saha and H. G. Tompkins, "Titanium nitride oxidation chemistry: An x-ray photoelectron spectroscopy study," J. Appl. Phys. **72**, 3072–3079 (1992).

[59]J. Colligon, H. Kheyrandish, L. Lesnevsky, A. Naumkin, A. Rogozin, I. Shkarban, L. Vasilyev, and V. Yurasova, "Composition and chemical state of titanium nitride films obtained by different methods," Surf. Coat. Technol. **70**, 9–17 (1994).

[60]M. Krawczyk, W. Lisowski, J. W. Sobczak, A. Kosiński, and A. Jablonski, "Studies of the hot-pressed TiN material by electron spectroscopies," J. Alloys Compd. **546**, 280–285 (2013).

[61]N. K. Ponon, D. J. Appleby, E. Arac, P. King, S. Ganti, K. S. Kwa, and A. O'Neill, "Effect of deposition conditions and post deposition anneal on reactively sputtered titanium nitride thin films," Thin Solid Films **578**, 31–37 (2015).

[62]K. Hansen, M. Cardona, A. Dutta, and C. Yang, "Plasma Enhanced Atomic Layer Deposition of Plasmonic TiN Ultrathin Films Using TDMATi and NH_3," Materials **13**, 1058 (2020).

[63]Y. Liu, Y. Wang, Y. Zhang, Z. You, and X. Lv, "Mechanism on reduction and nitridation of micrometer-sized titania with ammonia gas," J. Am. Ceram. Soc. **103**, 3905–3916 (2020).

[64]H. O. Pierson, *Handbook of Refractory Carbides and Nitrides: Properties, Characteristics, Processing and Applications* (William Andrew, 1996).

[65]Z. Lin, G. Zhan, X. Wang, M. You, B. Yang, X. Chen, W. Zhang, and J. Liu, "Titanium nitride thin film for temperature sensing and its conductive mechanism in the cryogenic region," Semicond. Sci. Technol. **33**, A398 (2018).

Journal of Vacuum Science & Technology A

ACCEPTED MANUSCRIPT

PLEASE CITE THIS ARTICLE AS DOI: 10.1116/6.0002288

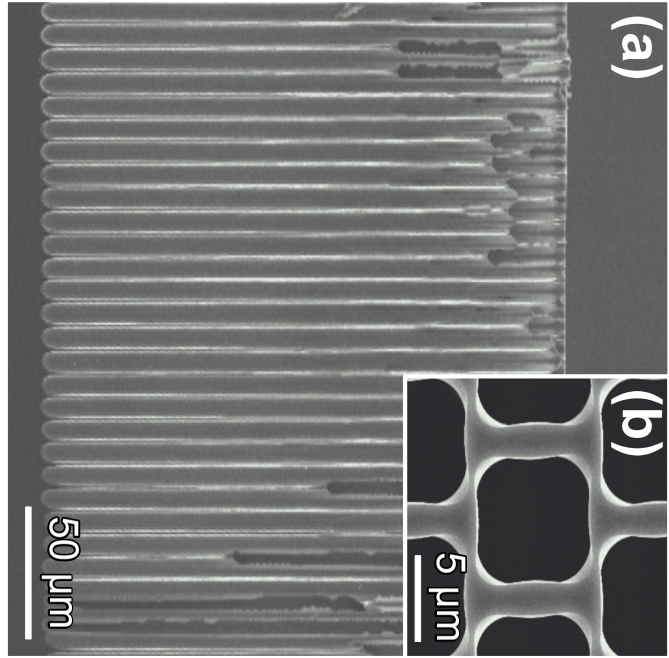

Journal of Vacuum Science & Technology A

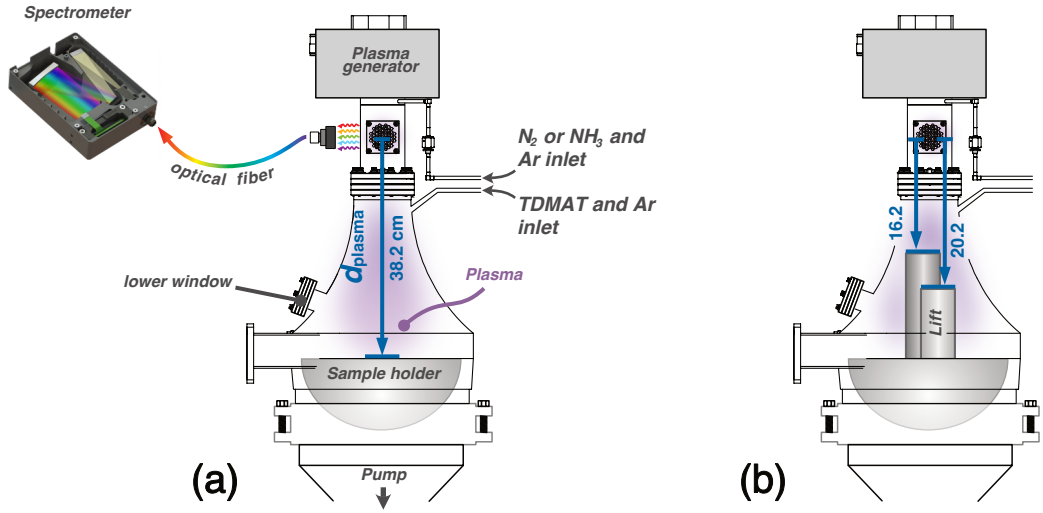

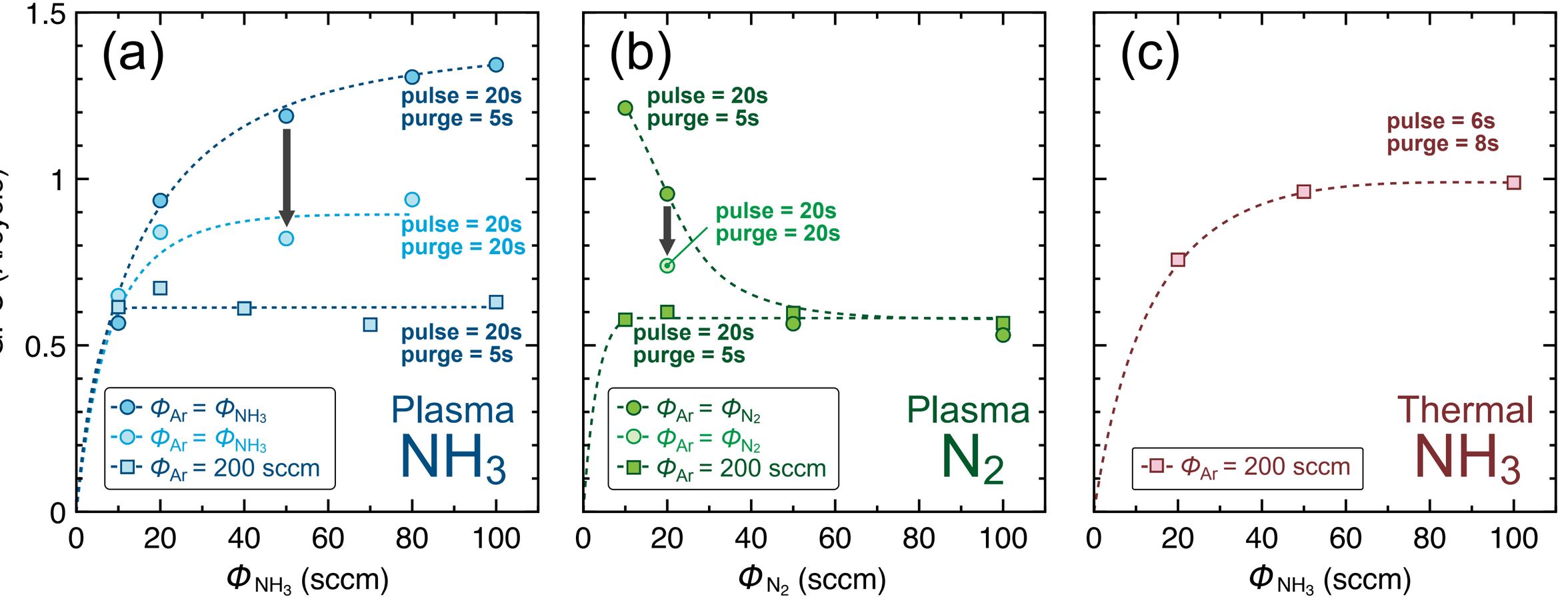

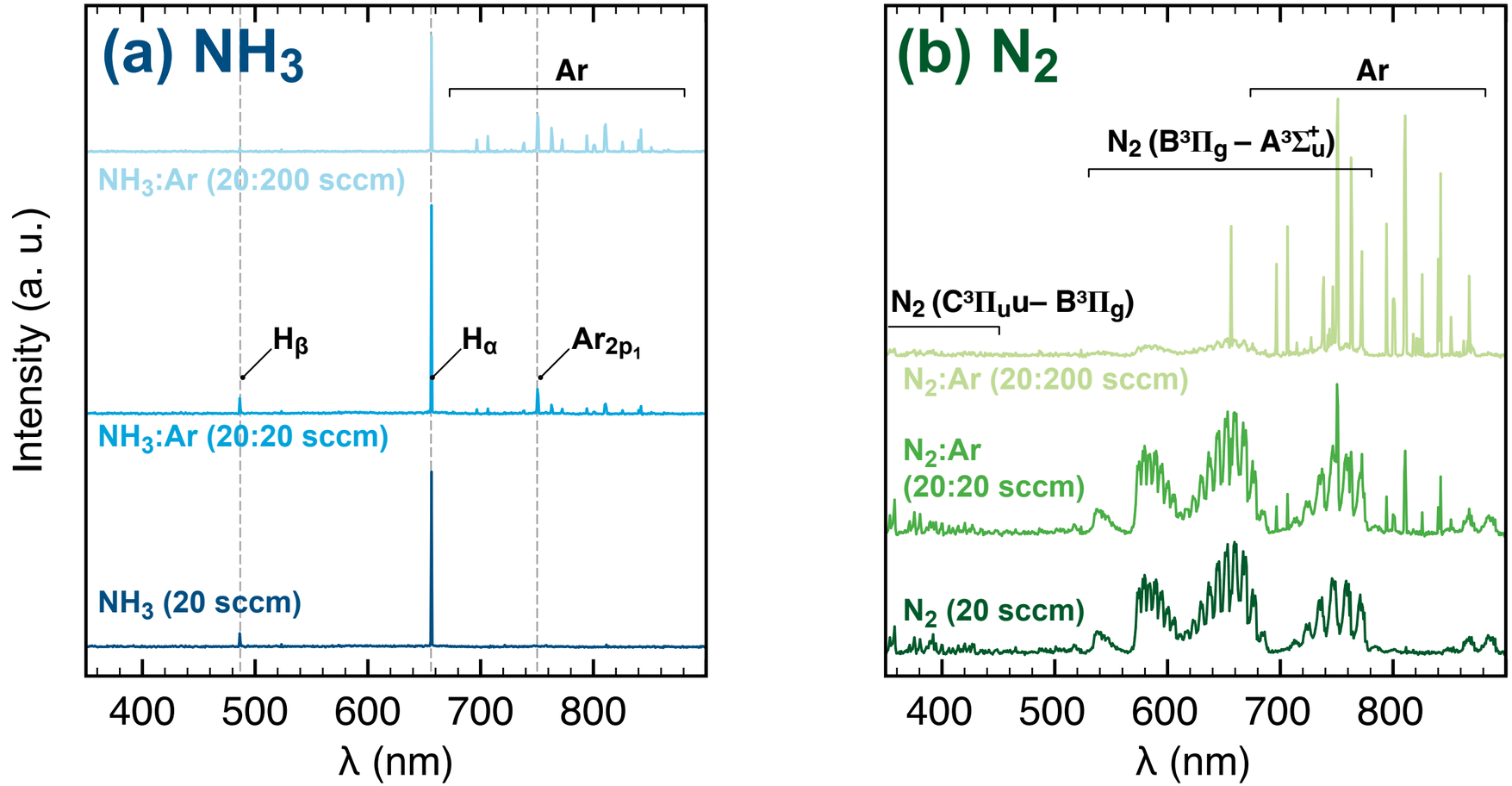

Journal of Vacuum Science & Technology A

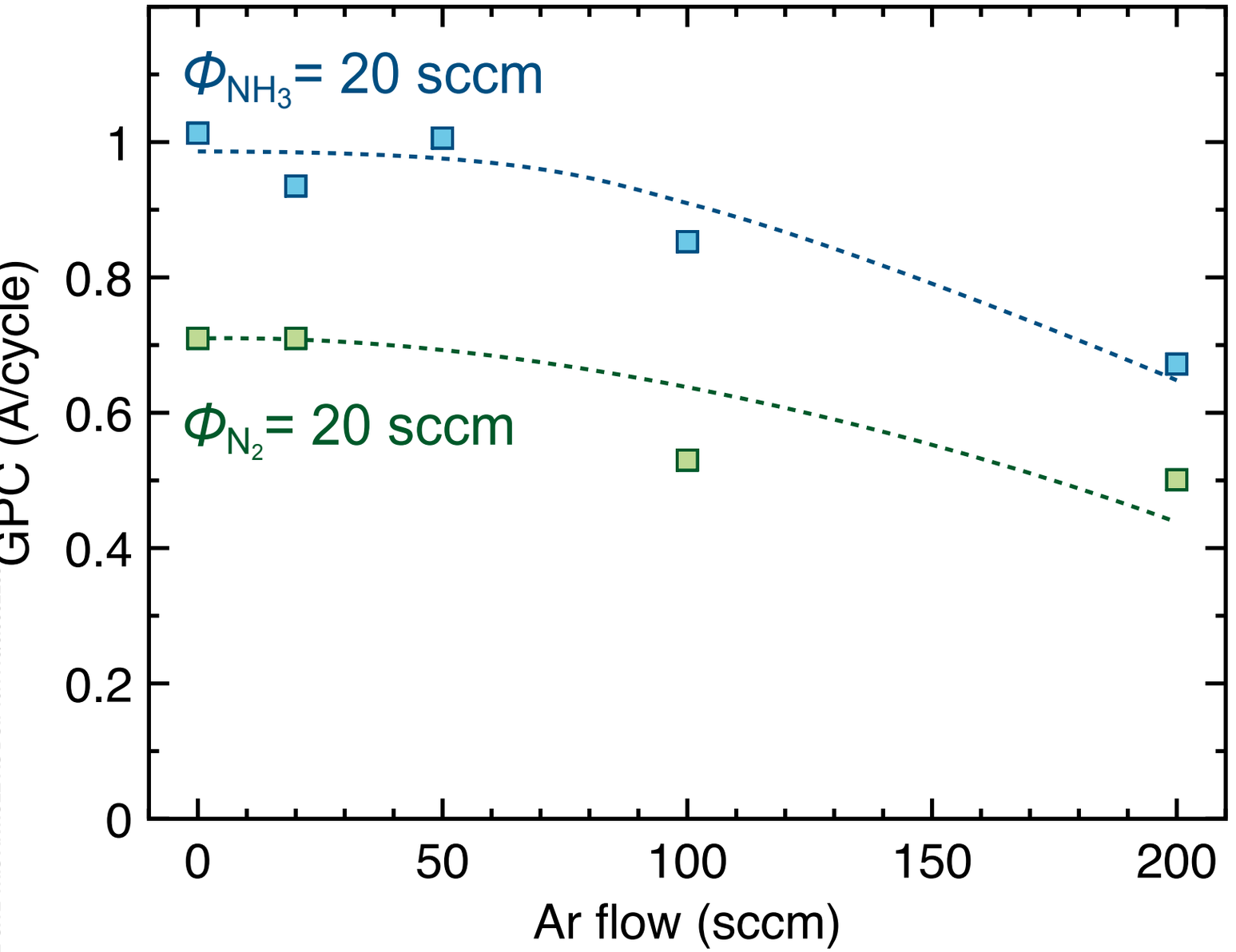

Journal of Vacuum Science & Technology A

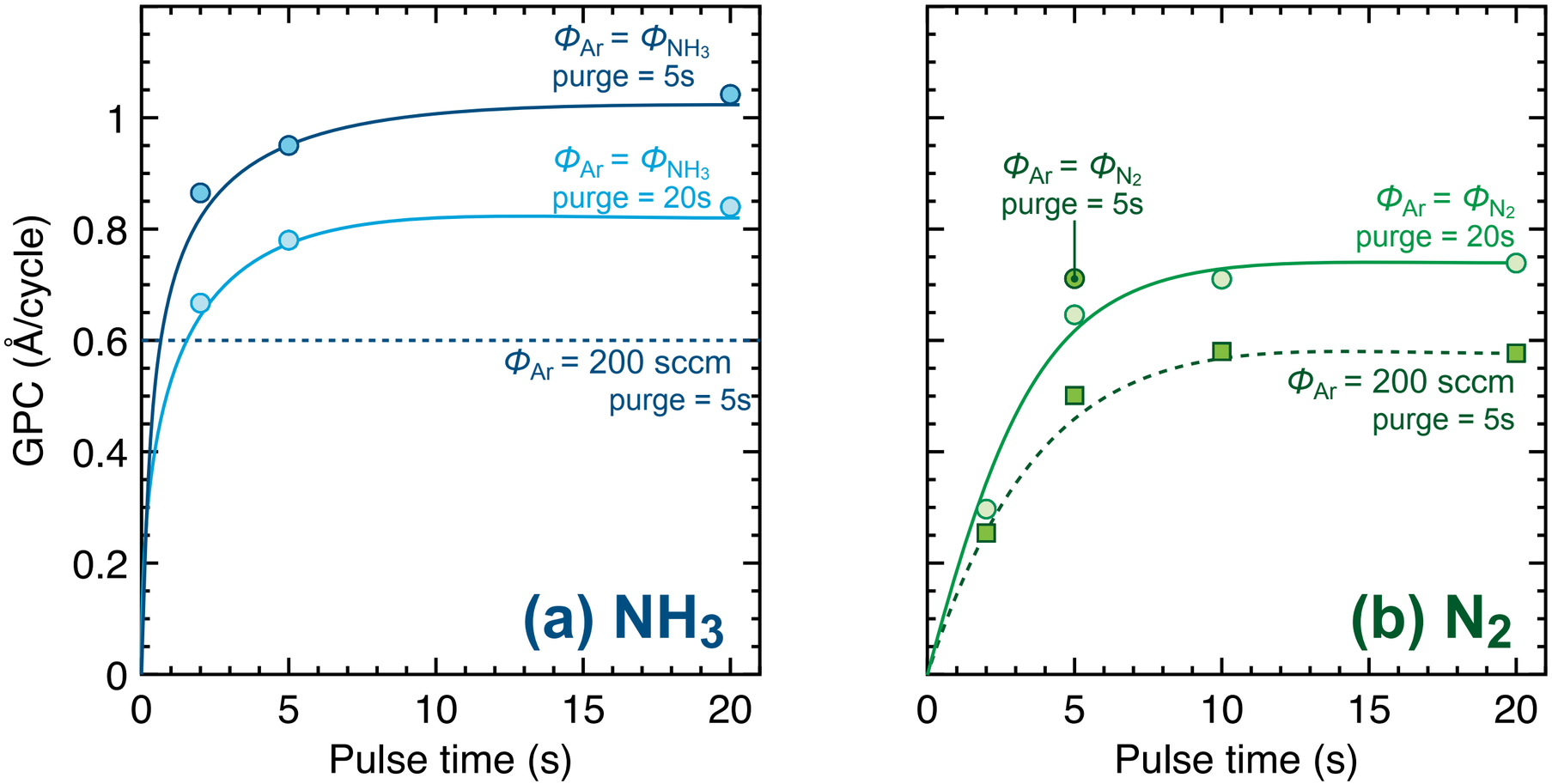

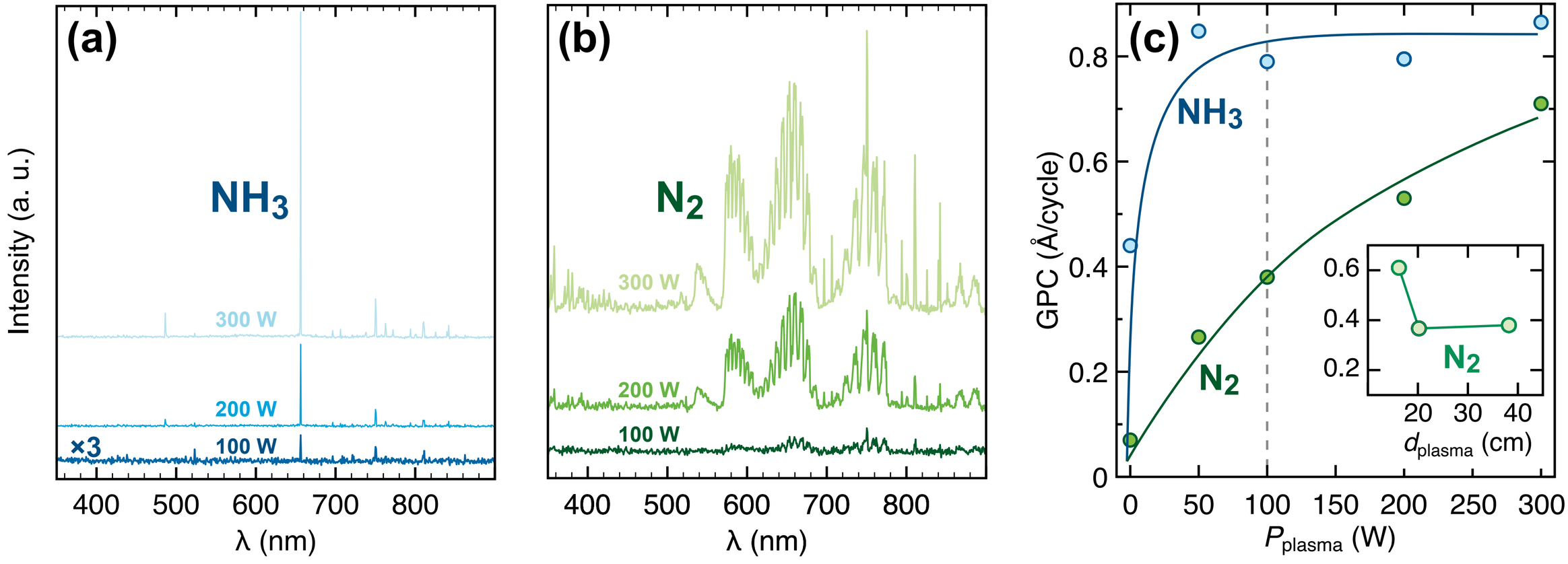

Journal of Vacuum Science & Technology A

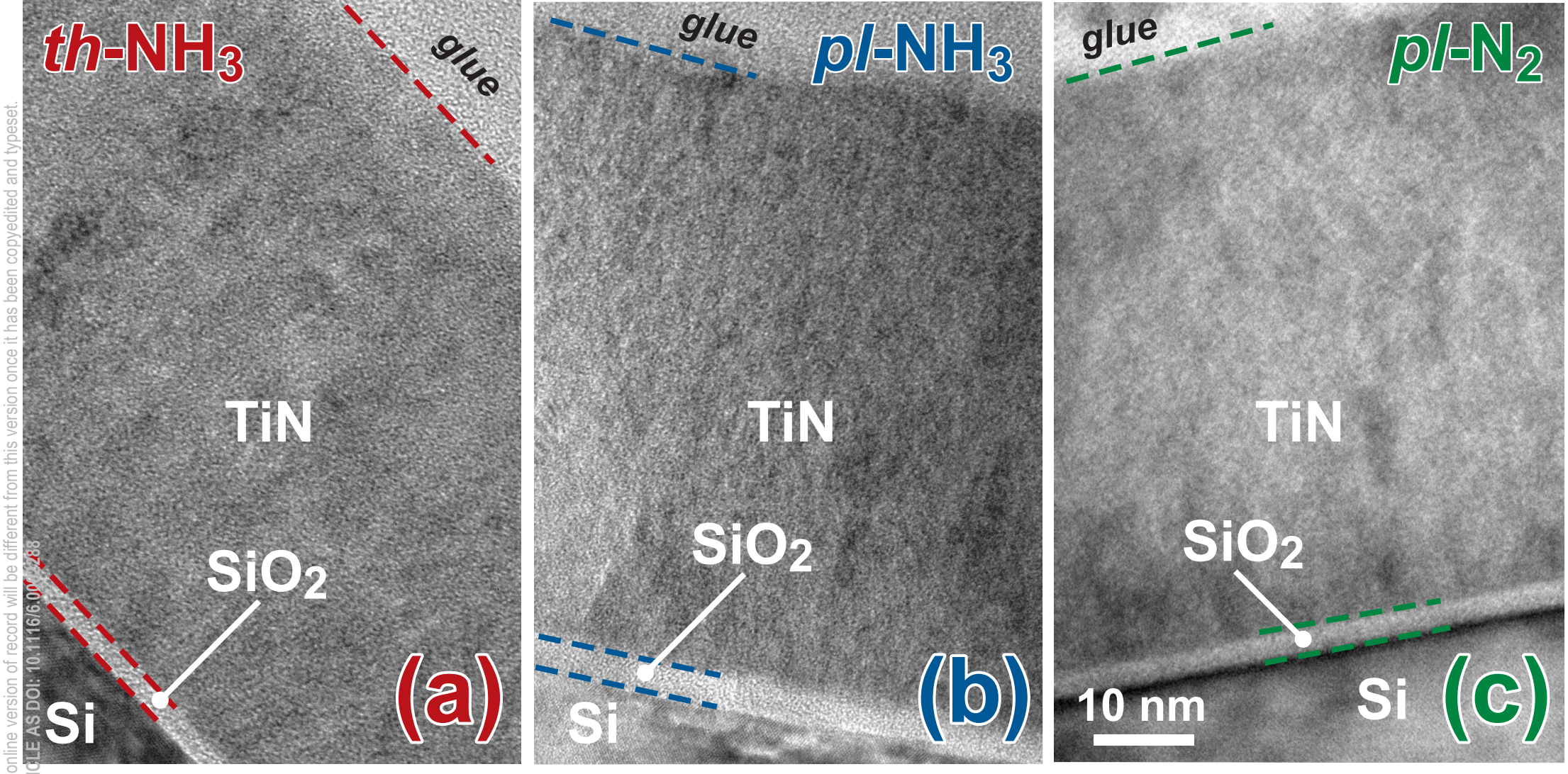

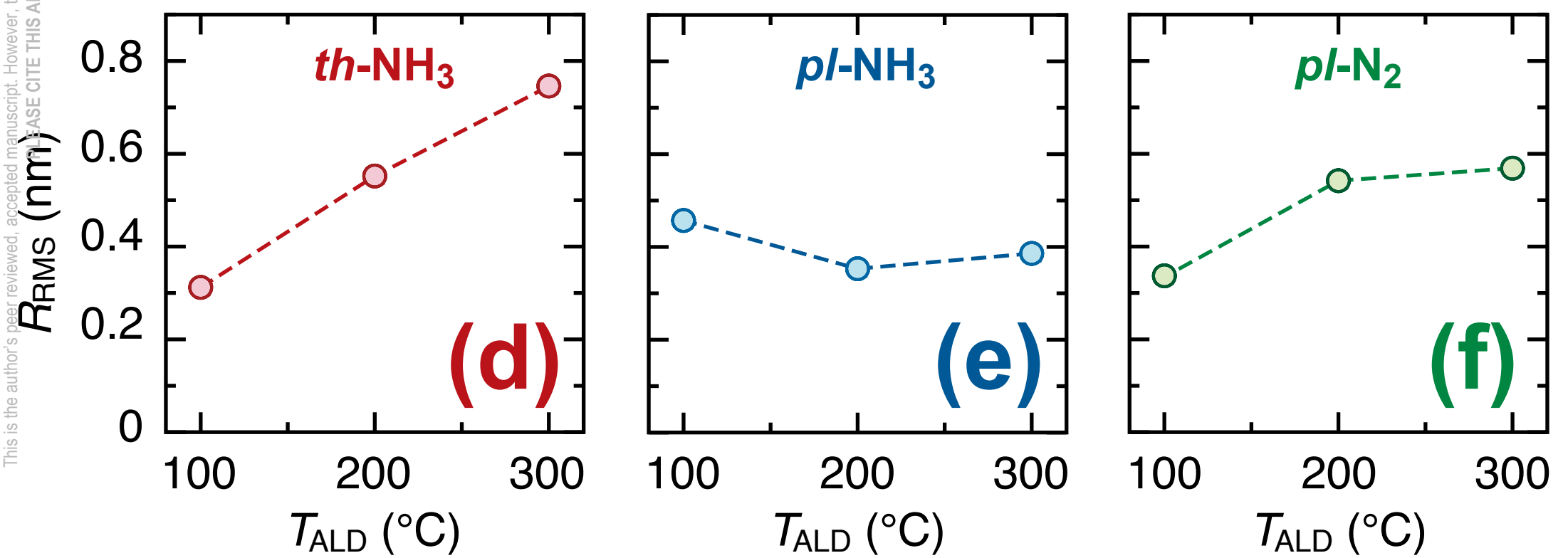

Journal of Vacuum Science & Technology A

PLEASE CITE THIS ARTICLE AS DOI: 10.1116/6.0002288

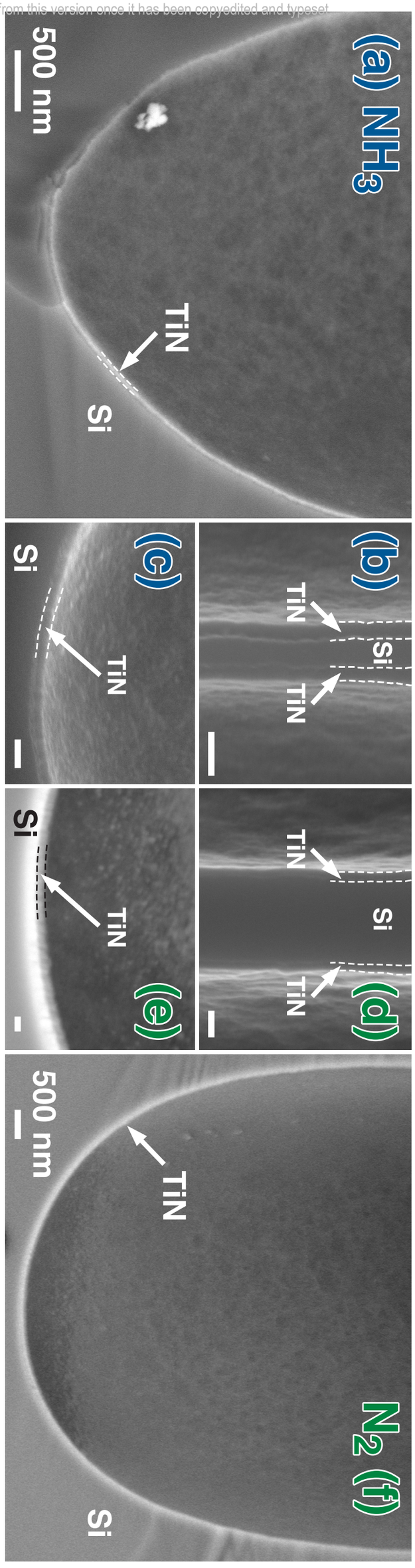

Journal of Vacuum Science & Technology A

PLEASE CITE THIS ARTICLE AS DOI: 10.1116/6.0002288

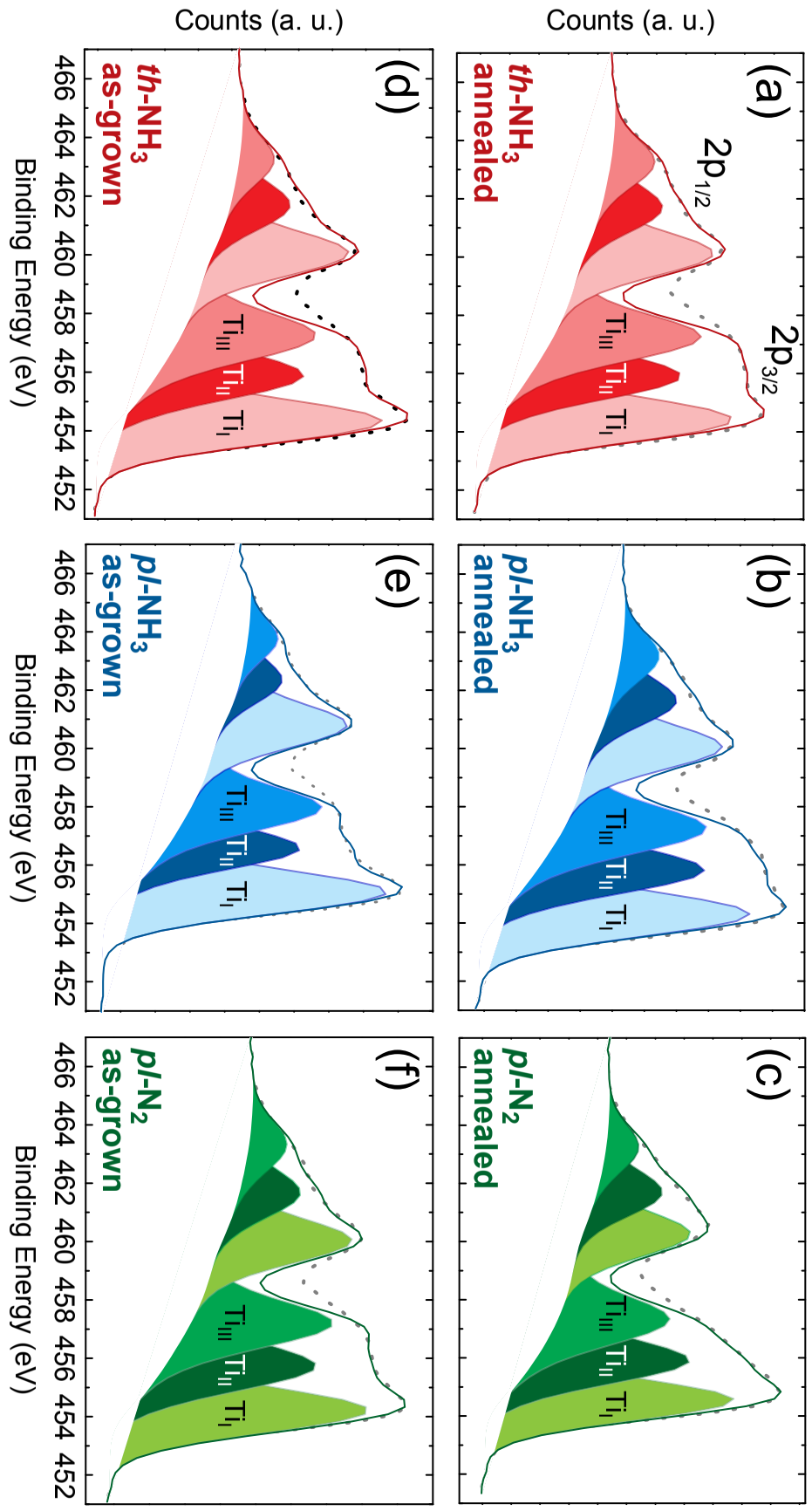

Journal of Vacuum Science & Technology A

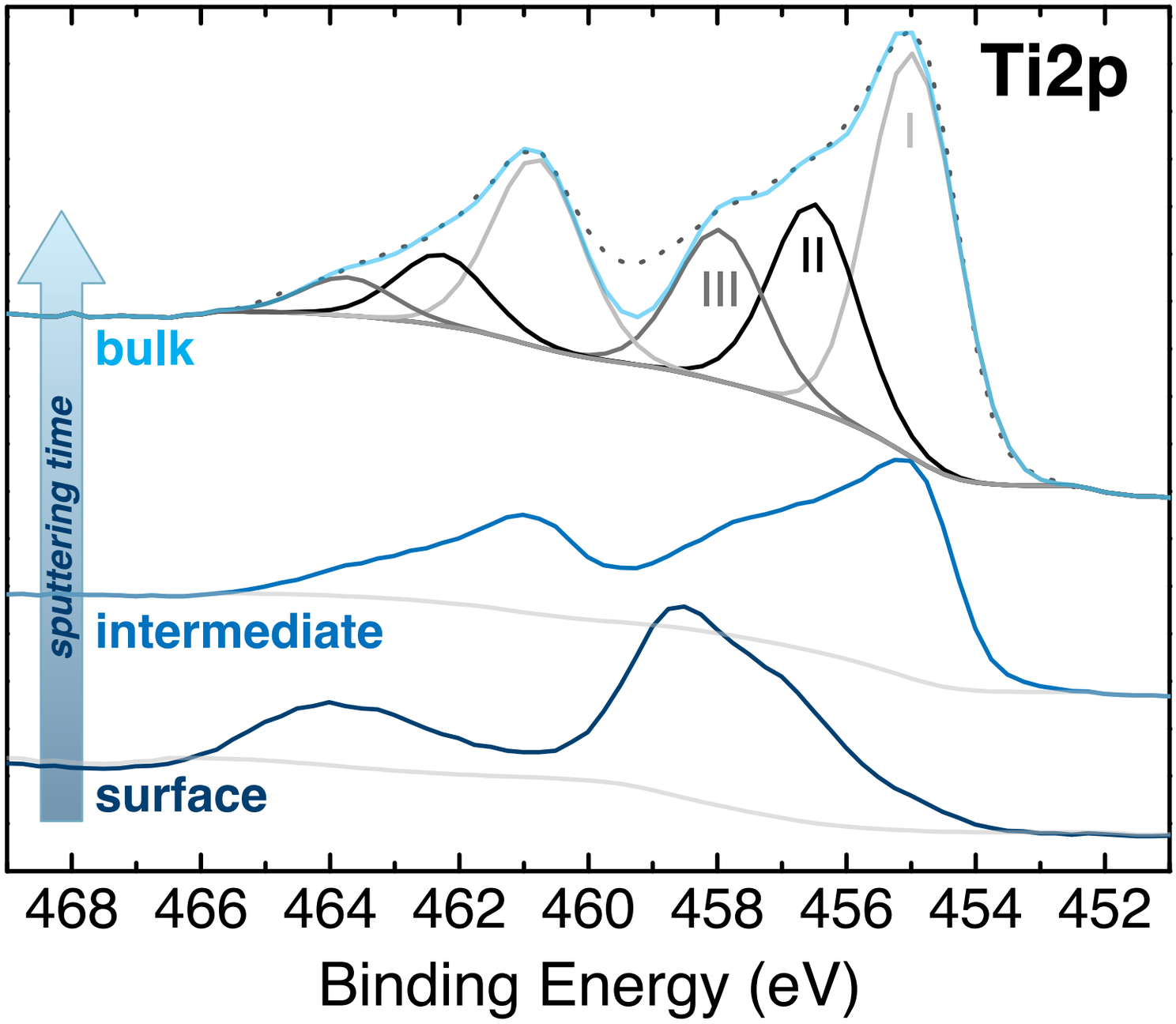

Journal of Vacuum Science & Technology A

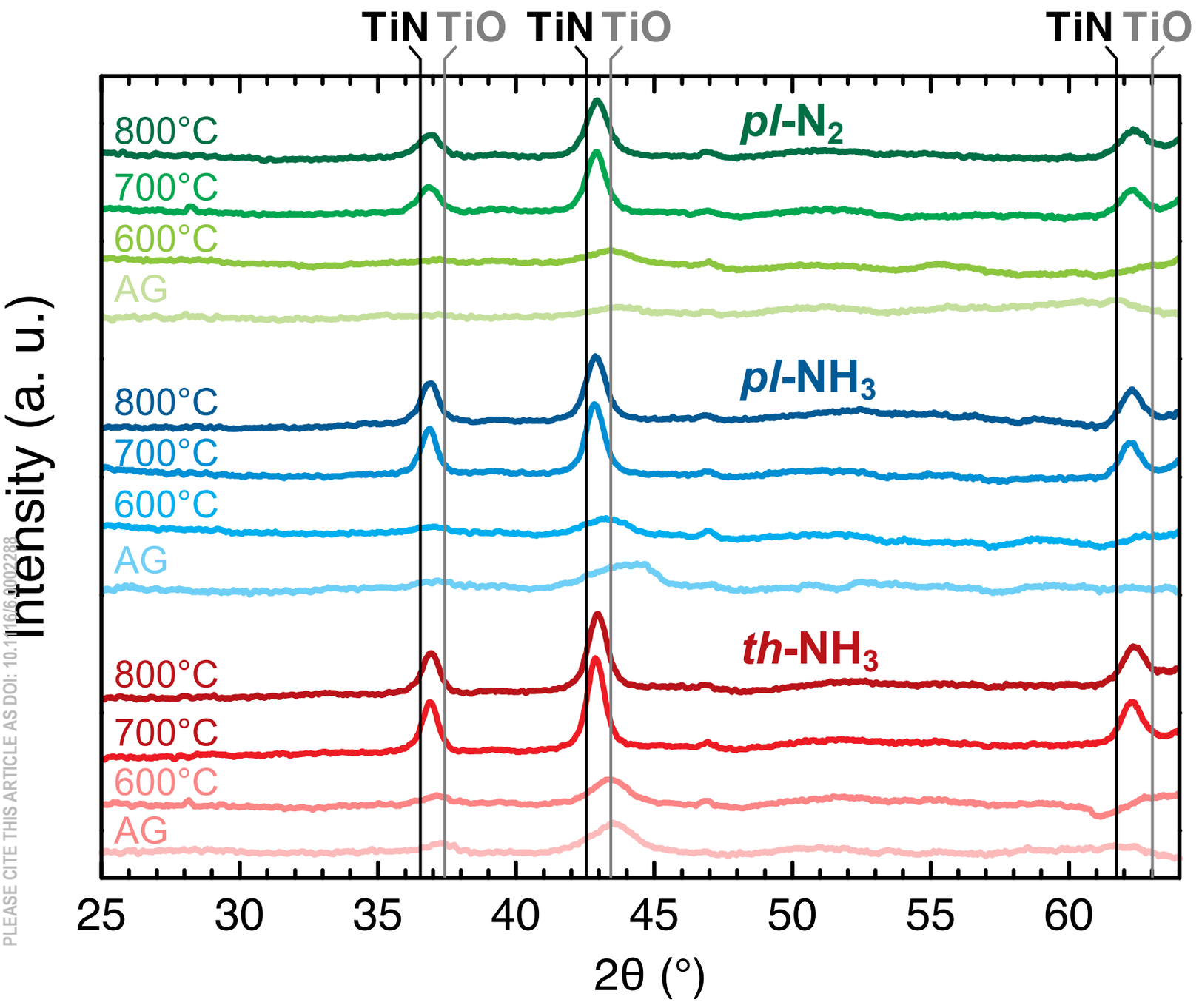

Journal of Vacuum Science & Technology A